

Mitochondria are absent from microglial processes performing surveillance, chemotaxis, and phagocytic engulfment

Received: 4 October 2024

Accepted: 13 November 2025

Published online: 12 December 2025

 Check for updates

Alicia N. Pietramale , Xhoela Bame , Megan E. Doty , Kiera E. Schwarz  & Robert A. Hill  

Microglia continually surveil the brain allowing for rapid detection of tissue damage or infection. Microglial metabolism is linked to tissue homeostasis, yet how mitochondria are subcellularly partitioned in microglia and dynamically reorganize during surveillance, injury responses, and phagocytic engulfment in the intact brain are not known. Here, we performed intravital imaging and ultrastructural analyses of microglia mitochondria in mice and human tissue, revealing that microglial processes diverge in their mitochondrial content, with some containing multiple mitochondria while others are completely void. Microtubules and hexokinase 2 mirror this uneven mitochondrial distribution indicating that these cytoskeletal and metabolic components are linked to mitochondrial organization in microglia. Microglial processes that engage in minute-to-minute surveillance typically do not have mitochondria. Moreover, unlike process surveillance, mitochondrial motility does not change with animal anesthesia. Likewise, the processes that acutely chemoattract to a lesion site or initially engage with a neuron undergoing programmed cell death do not contain mitochondria. Rather, microglia mitochondria have a delayed arrival into the responding cell processes. Thus, there is subcellular heterogeneity of mitochondrial partitioning. Moreover, microglial processes that surveil and acutely respond to damage do not contain mitochondria.

Microglia serve as the resident phagocyte of the central nervous system. They are a highly dynamic, innate immune cells capable of functions that span tissue surveillance to pathological responses^{1,2}. They do this by continually extending and retracting their extensively branched processes to probe the environment for infection or injury. In the case of a focal injury, microglia display immediate process chemotaxis, effectively barricading the injury site to prevent further damage to the parenchyma^{3,4}. Subsequent microglial phagocytosis mediates engulfment and clearance of cellular debris, ultimately facilitating a return to homeostasis from this inflammatory injury. Microglia also perform phagocytosis without inflammatory stimuli via specialized phagocytic receptors that recognize damaged or dying cells or cell compartments (efferocytosis)⁵⁻⁹. Together, surveillance,

chemotaxis, and phagocytosis involve radical morphological changes in microglia, but our understanding of how the internal cellular architecture changes alongside these cell behaviors is incomplete.

Mitochondria are signaling hubs involved in many processes ranging from cell metabolism, calcium handling, cell death and proliferation, and the generation of reactive oxygen species (ROS)^{10,11}. Mitochondrial subcellular localization influences these multifunctional roles and their proximity to other organelles or positioning near cell-cell contacts enhances their ability to integrate and respond to intracellular and extracellular stimuli¹⁰. Mitochondria are also dynamic organelles capable of transport throughout the cell mediated by the cytoskeleton, and changing shape through fission and fusion events, each of which have been linked to the metabolic state of the cell^{10,12-14}.

In aging and neurodegeneration, microglial function is dysregulated, potentially contributing to the pathology rather than helping the system return to homeostasis^{2,15–24}. In this state, microglia exhibit mitochondrial dysregulation shown by increased ROS emission, mitochondrial DNA damage, and metabolic dysfunction^{24–27}. Additionally, inflammatory environments alter mitochondrial shape in microglia in vitro, which coincides with a microglial bioenergetic shift and an increase in pro-inflammatory cytokine release^{28–31}. Moreover, targeted manipulation of distinct mitochondrial genes such as uncoupling protein 2 and hexokinase 2 within microglia has revealed diverse roles for mitochondria in microglial physiology and pathology^{32–36}. However, it remains to be explored how mitochondrial shape and motility change as microglia perform surveillance, phagocytosis, and respond to injury in the healthy brain.

In this study, we define the microglia mitochondrial dynamics at homeostasis to provide a baseline of the mitochondrial phenotype as microglia carry out their multifaceted functions. To investigate microglia mitochondria, we generated a triple transgenic mouse with microglia and their mitochondria endogenously labeled with separate fluorescent markers. This enables us to study mitochondrial morphology and motility in live animals while maintaining microglia in their native microenvironment. Together, our data establish the dynamics and morphometrics of microglia mitochondria in vivo, and indicate heterogeneity of process function within a single microglial cell.

Results

Mitochondrial morphometrics in mouse neocortical microglia

Inflammatory stimuli shift the bioenergetics of cultured microglia which coincides with a morphological change of mitochondria in microglia^{28–31}. However, mitochondrial morphometrics (content, shape, and subcellular distribution) and motility have not been characterized in microglia in the healthy, live, and intact brain. To visualize mitochondria specifically within microglia, we generated a triple transgenic mouse line, *Cx3cr1-creER*: Ai9: PhAM, enabling dual fluorophore expression in the cell cytoplasm (Ai9) and mitochondrial matrix (Dendra2) driven by tamoxifen-inducible Cre recombination (Fig. 1a, Supplementary Fig. 1a, b, and Supplementary Movie 1). We confirmed that Dendra2 reliably labeled the mitochondria in the cell by quantifying the overlap of Dendra2 and another mitochondrial marker, TOMM20 (95% overlap from 80 spots from 16 cells from 4 mice; Supplementary Fig. 2). These results are consistent with past reports of reliable labeling of mitochondria with this mouse line^{32,37,38}. To make the brain optically accessible for intravital imaging, cranial window surgeries were performed over the somatosensory cortex (Supplementary Fig. 1a). Immediately after the surgery, high resolution optical images were taken, then the microglia cytoplasm and mitochondria were 3 dimensionally (3D) segmented (Supplementary Fig. 1c). Using the volumes extracted from the 3D segmentations, we found the mitochondrial to cytoplasmic volume fraction in the whole cell and the compartments: soma and processes to be respectively -10%, 17%, and -8% (Fig. 1b). The soma contained relatively few but large mitochondrial networks by volume while the mitochondria occupying the processes were smaller in volume but greater in number (Fig. 1a, c). Mitochondrial shape was also determined within these cellular compartments with circularity and aspect ratio measurements as mitochondrial morphology has been correlated to metabolic fitness^{13,39}. The circularity of the soma and process mitochondria showed no difference; however, the aspect ratio showed that the process mitochondria were more elongated than the soma mitochondria (Fig. 1f).

To determine where mitochondria reside within microglia, Sholl analysis was done on the cytoplasmic and mitochondrial segmentations. The microglia branching complexity increased as the density of branching increased (peaking at ~20µm away from the cell center) and then dropped when moving to the tips of the processes, as

expected^{40,41}. However, this peak increase in complexity was not observed with the mitochondrial Sholl analysis, which linearly decreased when radiating away from the cell center to the tips of the processes (Fig. 1d). To measure this in a more detailed way, the mitochondrial occupancy in individual primary processes was determined. A primary process was identified from the branch shooting off from the soma and all connected branches (see primary processes labeled in different colors in Fig. 1e). Like the Sholl analysis, mitochondrial occupancy linearly decreased moving from the soma to the tips of the primary processes (Fig. 1e). Therefore, the complexity of the microglia cytoplasm does not dictate where there will be an increase in mitochondria presence. These analyses establish the baseline for mitochondrial morphometrics in the healthy intact brain, and can serve as a reference as to how mitochondrial morphometrics may change in neuroinflammatory and neurodegenerative states.

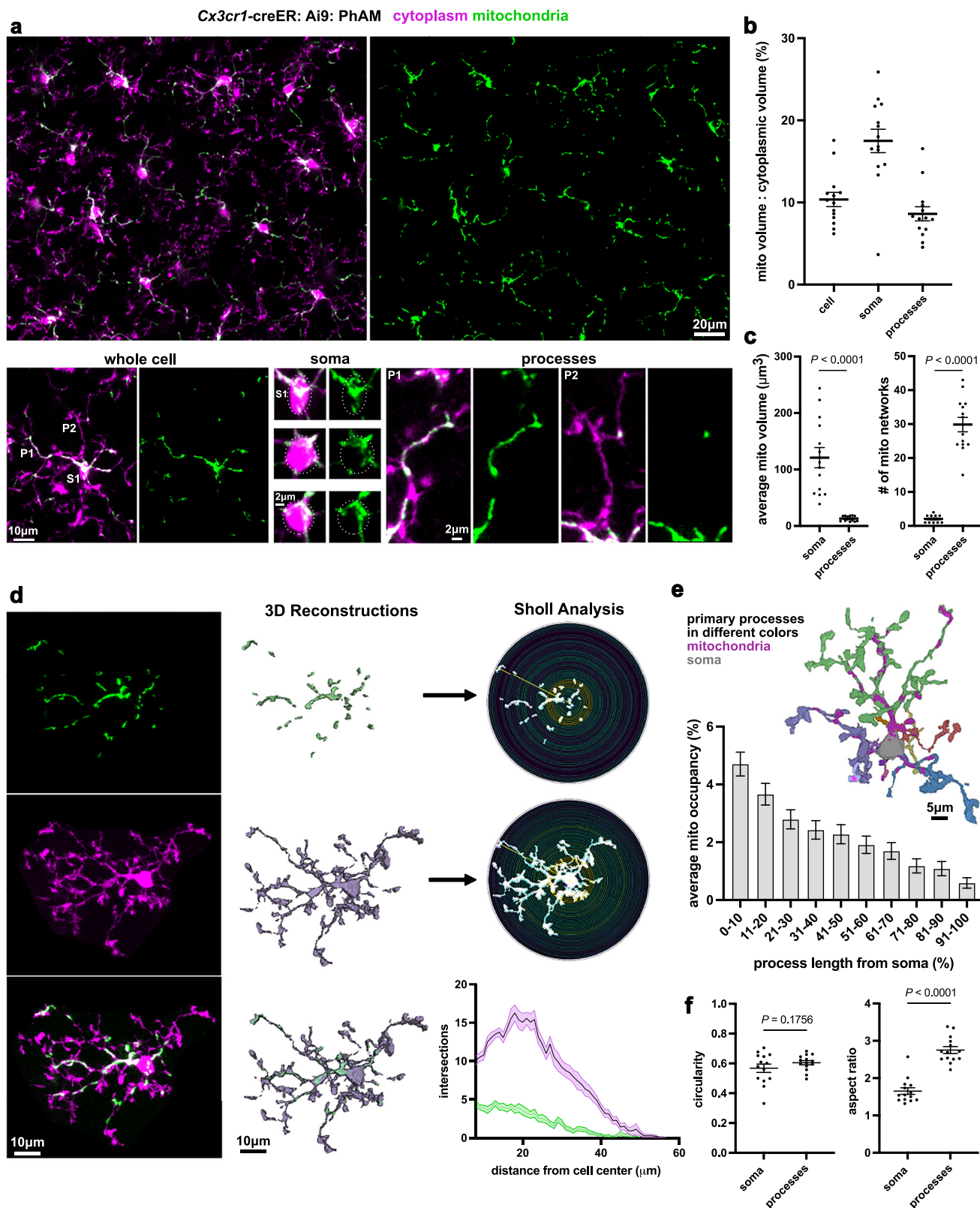
Mitochondrial morphometrics in human neocortical microglia

To determine if the microglial mitochondrial morphometrics were consistent across species, we used a publicly available human electron microscopy dataset (H01) that was collected from 1 mm³ of the temporal cortex⁴². We selected 6 microglia to segment, and confirmed their identity based on nuclear ultrastructure and cell cytoplasmic morphology⁴³. We then created 3D segmentations of the cytoplasm, nucleus, and mitochondria (Fig. 2a, Supplementary Fig. 7 and Supplementary Movie 2). The mitochondria to cytoplasmic volume fraction in the whole cell, soma, and processes was between 2.5% and 3.5% (Fig. 2a, d). We also found that the mitochondria in the soma were larger in volume but fewer in quantity, whereas the mitochondria in the processes were smaller in volume but greater in quantity (Fig. 2b, c, e). Moreover, the Sholl analysis showed that mitochondria are more abundant at the cell center and linearly decrease to less abundant at the process tips (Fig. 2f). Not only are these findings consistent with the mouse mitochondrial morphometrics, but this electron microscopy dataset also provides the resolution to distinguish individual mitochondria and validates our findings made with the resolution capabilities of fluorescence microscopy.

Mitochondria are heterogeneously partitioned throughout microglia processes

By qualitative observation it was apparent that some processes had little to no mitochondria, while other processes had many mitochondria in both mouse and human neocortical microglia (Fig. 3a, b and Supplementary Fig. 8a). To represent this quantitatively, the mitochondrial volume in each primary process was plotted against the primary process length, and indeed, primary processes from the same cell had similar lengths, but varied in their total mitochondrial volume (Fig. 3c). To determine if the mitochondrial shape differed in these primary processes, we used the mitochondrial volume to separate the primary processes in two groups, designating primary processes as having high (>67.1 µm³) or low (<67.1 µm³) mitochondrial volume (Fig. 3d). We then compared the shape of the mitochondria in each group. This analysis revealed that the primary processes with low mitochondrial volume had more circular mitochondria compared to processes with high mitochondrial volume that had more elongated mitochondria (Fig. 3e and Supplementary Fig. 8b). Given these data, mitochondria are not uniformly distributed in mouse or human microglia, raising the question of whether there are other structural differences between these processes.

To further analyze the heterogeneity of microglia processes, we used the H01 dataset to look at the proximity of microglia processes to other structures in the parenchyma. We focused on microglia process tips as reference points for distance measurements and discrete regions for comparison to mitochondrial content. Vasculature in the parenchyma is a prominent source of nutrients and energetic fuel. However, we found no correlation between mitochondrial content and



distance to blood vessels (Fig. 4a, b). Neurons are also key communication partners for microglia^{44,45}. Most of the microglia analyzed here formed soma-soma contacts with neurons, while those without soma-soma contacts were close to a neuron soma (Fig. 4c). We found no correlation between the distance from microglia soma to neuron soma and whole-cell mitochondrial content (Fig. 4d). Similarly, focusing on microglia process tips, no correlation was found between distance to

neighboring neuron soma and mitochondrial content (Fig. 4c, d). While this analysis only begins to address the extensive array of contacts between microglia and other cells (Fig. 4e), these data suggest that proximity to blood vessels or neuronal somas does not relate to the uneven partitioning of mitochondria in microglia.

Given the heterogeneous partitioning of mitochondria in microglial processes, we next hypothesized that mitochondria would be near

Fig. 1 | Mitochondrial morphometrics in mouse neocortical microglia. **a** In vivo image of mitochondrial labeling (green) in microglia (magenta) in the upper layers of the mouse somatosensory cortex. The images on the bottom show mitochondrial partitioning in 1 microglia (left image), representative soma from three separate microglia (middle images) and the two processes cropped from the first microglia as indicated and numbered. **b** The mitochondrial to cytoplasm volume fraction for a subset of microglia that were segmented in 3D. Values are shown for the total cell, the soma, and the processes. Each dot in the graph represents 1 cell. **c** Differences in the average mitochondrial network volume and number of mitochondrial networks between the soma and processes. **d** 3D segmentation of a single

microglia and its mitochondria and morphological analysis via Sholl reveals increased process complexity (magenta line) at 20 microns from the cell center but linear mitochondrial signals (green line) radiating from the center of the cell. **e** The mitochondrial occupancy along the length of a microglial primary process in 10% bins starting from the center of the cell (0–10%) and going to the tip of the process (91–100%) ($n = 117$ primary processes from 14 cells from 6 mice, error bars indicate s.e.m.) **f** Mitochondrial circularity and aspect ratio in the soma and processes. (for **b–f**, $n = 14$ cells from 6 mice, paired two-tailed t -test, the line is at the mean \pm s.e.m for error bars or error bands.) For (**b**, **c**, **f**), see Supplementary Figs. 3a–c and 5a–c for analyses by animal and of sex differences, respectively.

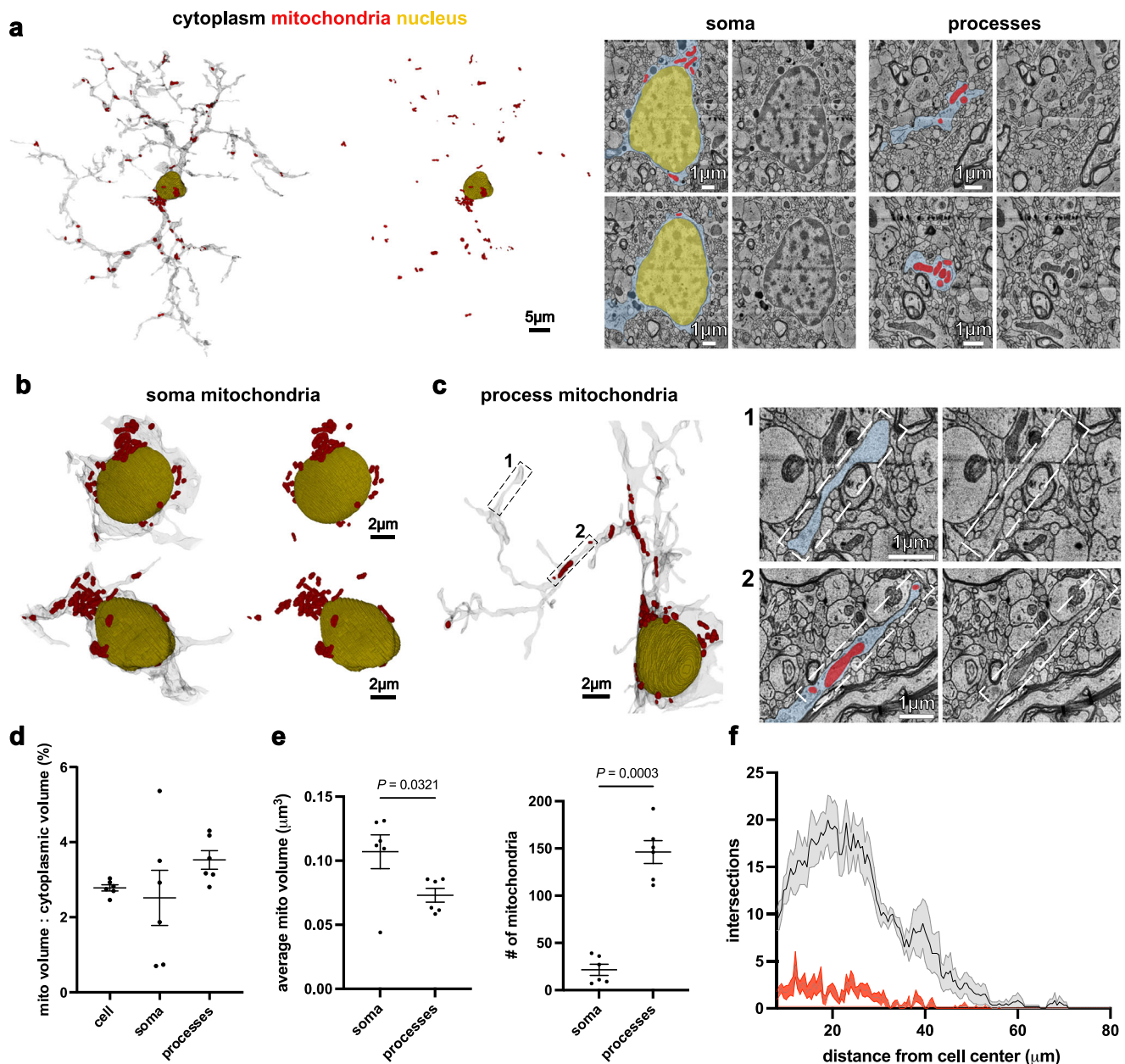
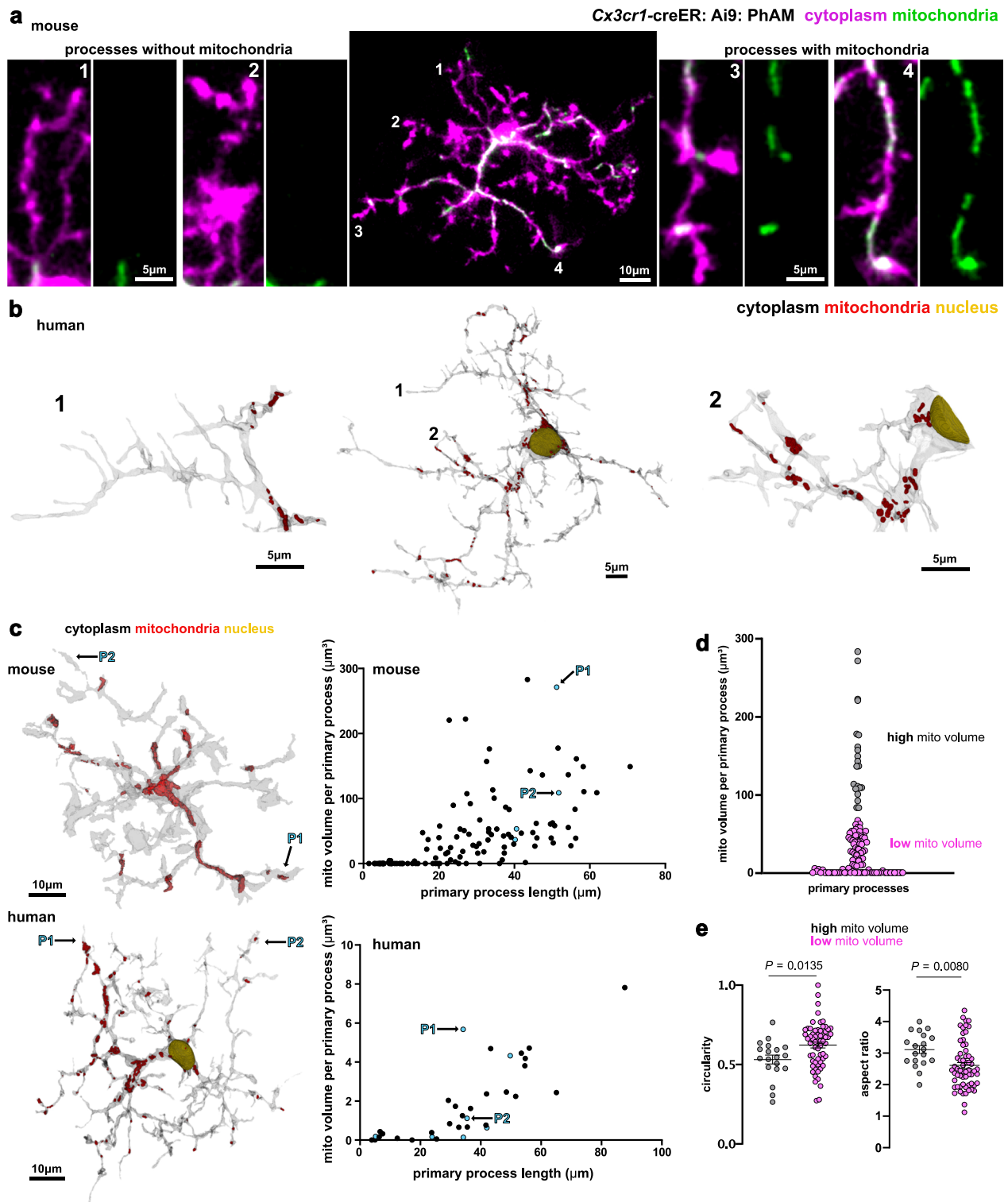


Fig. 2 | Mitochondrial morphometrics in human neocortical microglia. **a** 3D reconstruction of a microglial cell (gray or blue), its nucleus (yellow), and all its mitochondria (red) taken from a sample of human neocortex. The images on the right show examples of electron micrographs taken through the soma or single processes that were used for cell and organelle segmentations. **b** 3D renderings of microglial soma showing examples of perinuclear mitochondria. **c** Some microglial processes contain many mitochondria and others are completely void as shown by the reconstruction (left) and the electron micrographs (right) of the indicated

regions. **d** The mitochondrial to cytoplasm volume fraction for the microglia that were segmented in 3D. Values are shown for the total cell, the soma, and the processes. Each dot in the graph represents 1 cell. **e** Differences in the total mitochondrial volume and number of mitochondrial networks between the soma and processes (paired two-tailed t -test). **f** Sholl analysis reveals increased process complexity (gray line) at 20 microns from the cell center but linear mitochondrial signals (red line) measured from the center of the cell. For (**d–f**), $n = 6$ cells, error bars or bands indicate mean \pm s.e.m).



microtubules (MTs) since they are involved in mitochondrial anchoring, transport, and function^{13,46–48}. To visualize MTs in parallel with the cytoplasm and mitochondria, we generated a triple transgenic mouse line, *Cx3cr1*-creER: Ai9: Kaleidoscope, enabling triple fluorophore expression in the microglial cytoplasm (Ai9), mitochondrial matrix (mKate2), and MTs (eGFP) (Fig. 5a). Intravital 2-photon imaging showed that MT and mitochondrial localization in microglia was comparable with some microglial processes containing a robust MT network and others completely lacking microtubules and mitochondria (Fig. 5). Quantification revealed that MTs were more likely to be present in

microglial processes that contained mitochondria (Fig. 5e). These findings reveal that MTs likely influence how mitochondria are heterogeneously partitioned in some microglial processes and not in others.

Hexokinase 2, but not hexokinase 3, localizes to mitochondria in microglia

Having established that cytoskeletal differences underly the asymmetric distribution of mitochondria, we next considered the role of metabolic proteins. Specifically, we determined the distribution of hexokinase 2 (HK2) and 3 (HK3) in microglia. Hexokinase is required

Fig. 3 | Mitochondria are heterogeneously partitioned throughout microglial processes. **a** In vivo image of 1 microglia from the mouse cortex (center image) with single regions cropped that represent processes without mitochondria (left images) and with mitochondria (right images) as indicated by number labels 1–4. **b** 3D rendering of 1 human cortical microglia (center image) from EM segmentations of microglial cytoplasm (gray), mitochondria (red), and nucleus (yellow). Cropped images of processes 1 and 2 represent little to no mitochondria (left image) and many mitochondria (right image), respectively. **c** 3D renderings of in vivo (top) and EM (bottom) microglia with respective scatter plots of the total mitochondrial volume in each primary process against the primary process length. All dots in the plots represent 1 primary process. Blue dots show the mitochondrial volume in the primary processes of the 3D rendered microglia. Primary processes

containing relatively high mitochondrial volume (P1) and low mitochondrial volume (P2) are indicated in the 3D renderings and the graphs. In vivo data, $n = 117$ primary processes from 14 cells from 6 mice. EM data, $n = 34$ primary processes from 6 cells from 1 human. **d** Primary processes from the in vivo data were designated with high ($>67.1 \mu\text{m}^3$, 19 primary processes) or low ($<67.1 \mu\text{m}^3$, 98 primary processes) mitochondrial volume by k-means clustering ($k = 2$; $n = 117$ primary processes from 14 cells from 6 mice). **e** Mitochondrial circularity and aspect ratio in primary processes with high ($n = 19$ primary processes) and low ($n = 62$ primary processes) mitochondrial volume. Primary processes lacking mitochondria were excluded from the analysis (unpaired two-tailed t-test, the line is at the mean \pm s.e.m for error bars). For **e** see Supplementary Figs. 3d and 5d for analyses by animal and of sex differences, respectively.

for the first step of glycolysis, and the HK2 isoform has been gaining traction in the microglia field due to its relevancy in neuroinflammation and neurodegeneration^{33,49–55}. HK2 and HK3 are two isoforms of hexokinase family that are highly expressed by microglia relative to other cells in the mouse CNS; human microglia are also selective expressors of HK2, but not HK3^{56,57}; therefore, these were ideal candidates to begin understanding what metabolic components may be connected to heterogenous partitioning of mitochondria in microglia. To determine hexokinase subcellular localization in microglia we immunostained for HK2 and HK3 in fixed brain tissue (Fig. 6a, b). First, the mitochondrial to cytoplasmic area fraction confirmed there was heterogenous distribution of mitochondria in microglia (Fig. 6c), corroborating our previous findings that were obtained from intravital optical imaging immediately after the cranial window surgery (Fig. 3). Visually, it was apparent that HK2 specifically localized to microglia, while HK3 expression is more widespread (Fig. 6a, b). Quantitatively, we found that HK2, but not HK3, had significantly more signal localized to microglial processes with high mitochondrial occupancy (Fig. 6a, b, d). Moreover, 75% of mitochondria co-localized with HK2, while only 7% of mitochondria co-localized with HK3 (Fig. 6a, b, e). These data show that HK2 localizes to mitochondria in microglia while HK3 is more widely expressed by other cells in the CNS and lacks specificity within the microglial cytoplasm. Thus, cytoskeletal and metabolic components also have heterogenous partitioning in microglia, supporting the notion that microglial processes of the same cell may carry out different functions simultaneously.

Microglial branches and process tips lacking mitochondria are more motile

To investigate mitochondrial localization and microglial process behavior, we next assessed mitochondrial positioning and motility as microglia carry out their canonical surveillance behavior. To do this, mice were imaged every 1 min for 30 min to enable minute-to-minute tracking of mitochondria in microglia (Fig. 7). First, the stability of 100 branches across 25 cells was assessed. A tracked branch defined as “stable” was present at 0 min and 30 min, and a “lost” branch was present at 0 min, but gone at 30 min. Twenty-eight percent of branches were lost, and 72% were stable (Fig. 7a). Of all branches assessed at 0 min, half contained mitochondria (Fig. 7a). Notably, there was a greater percentage of lost branches that did not have mitochondria (Fig. 7a, Supplementary Movie 3), suggesting that processes lacking mitochondria are more motile. Since much of the surveillant motility occurs at the tips of processes^{1,58} we quantified the number of tips that contain mitochondria and found that only 18% have mitochondria, supporting the idea that mitochondria are less likely to be present in motile processes (Fig. 7b). In support of this, quantification of the total distance traveled and instantaneous velocity for a subset of microglial process tips showed that processes without mitochondria moved more (Fig. 7c). Process tips that did have mitochondria were either stable for the entirety of the imaging session or retracted, but were never observed to extend (Fig. 7c).

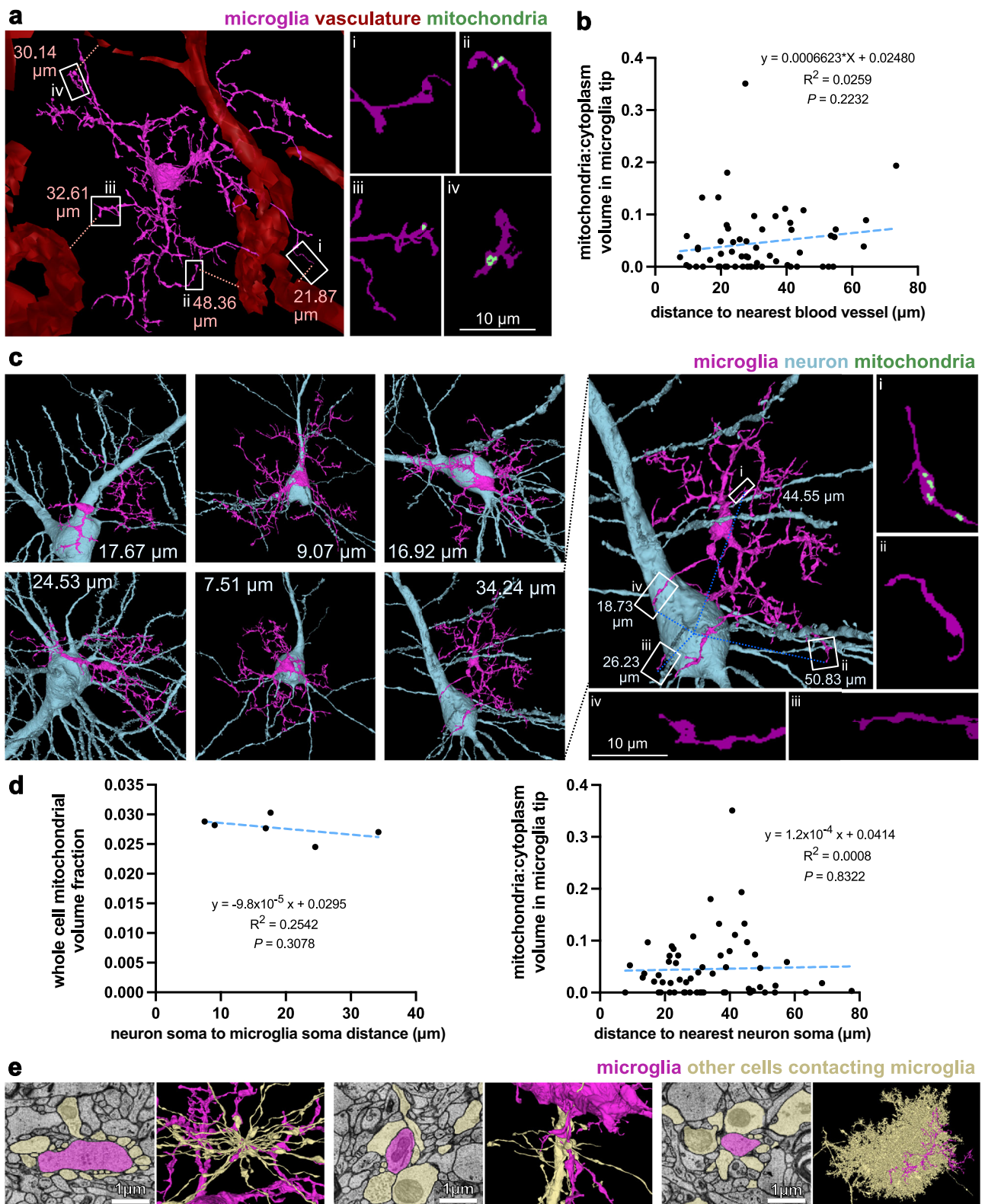
Next, to further determine overall mitochondrial motility vs. rearrangement of the microglial cytoplasm, we quantified the percent increase in area taken up by the cytoplasm and mitochondria at 0 min and in a temporal projection containing all 30 time points (seen as 0→30 min in Fig. 7d). The mitochondria to cytoplasmic fraction significantly decreased in the temporal projection compared to 0 min (Fig. 7d, e). Comparably, the percent change in area fraction of only the cytoplasm (60%) is significantly greater than the mitochondrial percent change in area fraction (37%) (Fig. 7d, f). Together, mitochondrial motility does not match the microglia process motility, suggesting that mitochondria are not often associated with processes that are performing tissue surveillance, particularly with regards to process extension.

Mitochondrial motility in microglia is not altered by animal anesthesia

Past work has shown that microglia surveillance behavior changes under different physiological states^{59,60}. Based on this, we reasoned that if mitochondrial motility is associated with microglial process motility, then a change in mitochondrial motility would be correlated with a change in brain physiological state. Thus, we next determined if different physiological states also alter mitochondrial motility in microglia. To do this, we imaged mitochondrial motility in the same microglia as mice transitioned from awake to anesthetized conditions. Animals were first imaged awake for 30 min, then switched to isoflurane anesthesia and imaged for another 30 min (Fig. 8a, c). The change in process area fraction showed that microglia were significantly less motile during wakefulness compared to when the mice were under isoflurane anesthesia (Fig. 8a, b and Supplementary Fig. 9), consistent with previous reports^{59,60}. However, mitochondrial tracking showed that the mitochondrial displacement and percentage of motile mitochondria were both unchanged in the awake and anesthetized conditions (Fig. 8d and Supplementary Movie 4). Thus, arousal state does not affect mitochondrial motility, again suggesting a disconnect between microglial process surveillance and mitochondrial motility.

Microglial processes acutely responding to a laser lesion do not contain mitochondria

Given that mitochondria were often not found in surveillant motile microglia processes, we next assessed mitochondrial motility in the context of microglial pathological response to acute tissue damage by a laser lesion. A 30 min time-series was acquired before the laser lesion, and immediately after the lesion a 45 min time-series was taken to capture the microglia and mitochondrial response to the lesion (Fig. 9). To quantify the response, the changes in fluorescence of the cytoplasmic and mitochondrial signals were measured in a region of interest (ROI) around the lesion site (Fig. 9a, b). As expected^{1,3}, multiple microglia processes immediately responded to the laser lesion; these processes arrived around the lesion site within minutes and sustained their presence for hours (Fig. 9c–e and Supplementary Movie 5).



Unexpectedly, mitochondria were not in the processes that responded to the lesion within the 45 min time frame (Fig. 9c–e and Supplementary Movie 5). To determine if mitochondria arrive later, an image was taken at 1 h and 6 h after the lesion. At 1 h, there were still little to no mitochondria at the lesion site (Supplementary Fig. 10), but at 6 h mitochondria occupied the processes extending to the lesion site (Fig. 9c–e). Therefore, microglial processes that immediately chemotax to the site of acute tissue damage do not have mitochondria,

rather, the mitochondria have a delayed arrival into the processes responding to the lesion.

Mitochondria are delayed in their arrival to microglial processes engulfing dying neurons

Finally, we investigated the mitochondrial dynamics and subcellular localization when single microglia clear apoptotic neurons. Targeted two-photon chemical apoptotic ablation (2Phatal) involves

Fig. 4 | Mitochondrial volume is not a predictor of microglial process proximity to blood vessels or neuron somas. **a** 3D reconstructions of microglia (magenta), vasculature (red), and mitochondria (green) from a sample of human neocortex. Left image: white boxes represent examples of microglia tips and their distance to the nearest blood vessel. Images on the right (i–iv) show max projected segmentations of microglia cytoplasm and mitochondria for each microglia tip. **b** No correlation between mitochondrial occupancy in the microglia tip and the distance to the nearest blood vessel. Each dot represents a microglia tip (n = 59 tips from 6 microglia). Blue dashed line represents the best-fit simple linear regression. **c** Left 6 images: depict the nearest neuron (light blue) to each of the 6 microglia (magenta) analyzed from the human neocortex. The values indicate the distance between

central points of microglia and neuron somas. Right images: an enlarged 3D reconstruction of a microglia and neuron showing how microglial tip distance from the neuronal soma was determined (dotted dark blue lines). Images i–iv show max projected segmentations of microglia cytoplasm and mitochondria for each microglia tip. **d** Left graph shows no correlation between the mitochondrial occupancy in microglia and the distance between microglia and neuron somas (n = 6 microglia). Right graph shows no correlation between mitochondrial occupancy in the microglia tip and the distance to the neuron soma (n = 59 tips from 6 microglia). Blue dashed lines represent the best-fit simple linear regression. **e** Three examples of electron micrographs showing segmentations and 3D reconstructions of all cells contacting a microglia process at a single z-plane.

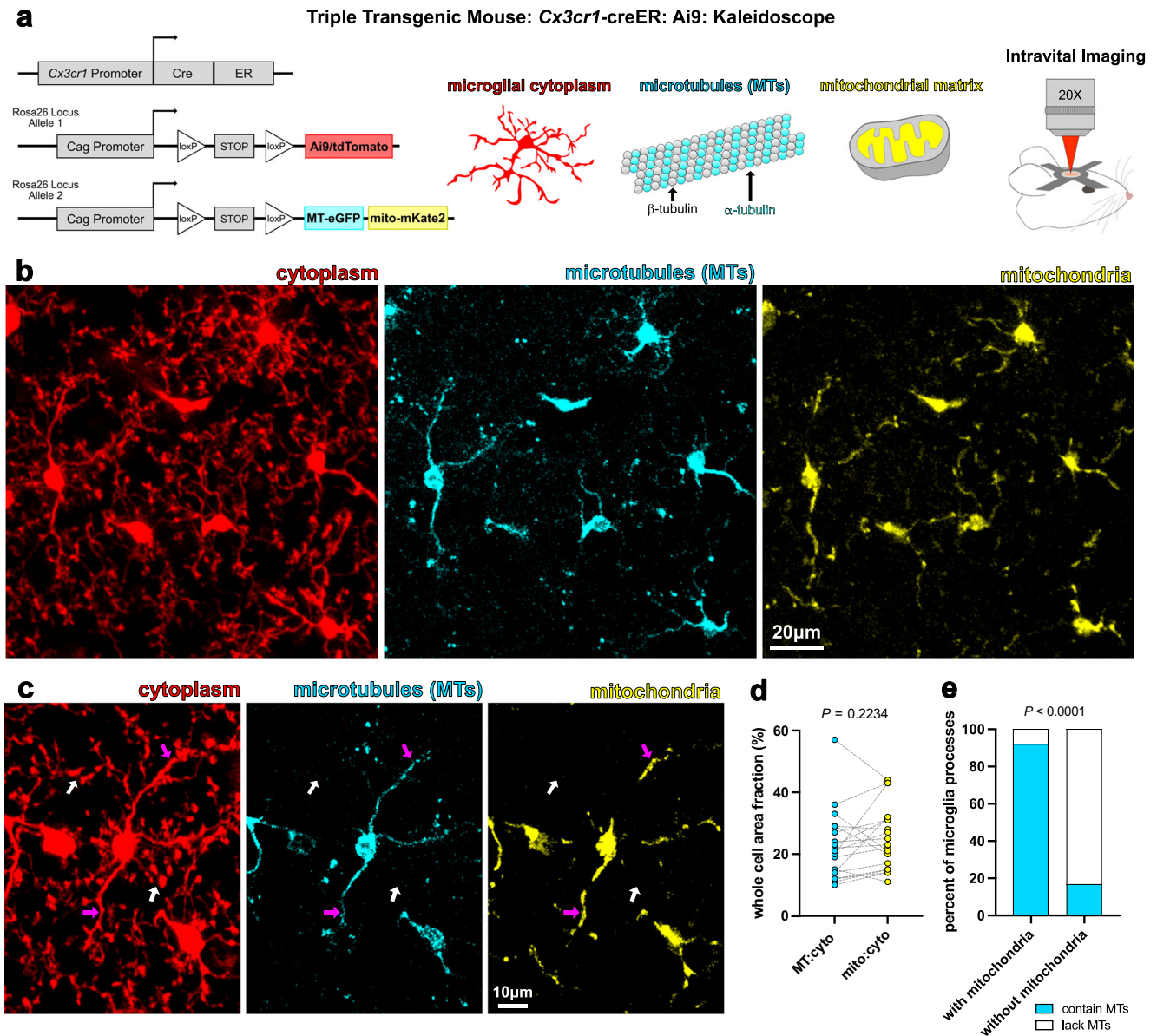


Fig. 5 | Microglial microtubule networks mimic the heterogeneous partitioning of mitochondria. **a** Strategy for Cre recombinase dependent conditional labeling and imaging of microglial cytoplasm and their microtubules (MTs) and mitochondria using floxed tdTomato, eGFP, and mKate2 fluorescent reporters, respectively. **b** Microglial cytoplasm (red), MTs (cyan), and mitochondria (yellow) were visualized in vivo using cranial window surgeries and intravital 2-photon imaging. **c** Representative microglia showing processes containing both MTs and

mitochondria (magenta arrows) and processes lacking both (white arrows). **d** Comparing area fraction of MTs and mitochondria in single microglia (n = 19 microglia from 5 mice; paired two-tailed t-test). **e** Binary analysis showing the percentage of processes with and without mitochondria that contain MTs (n = 24 processes with mitochondria and 24 processes without mitochondria from 12 microglia and 6 mice; two-sided Fisher's exact test). For (d, e) see Supplementary Figs. 3e and 5e, f for analyses by animal and of sex differences, respectively.

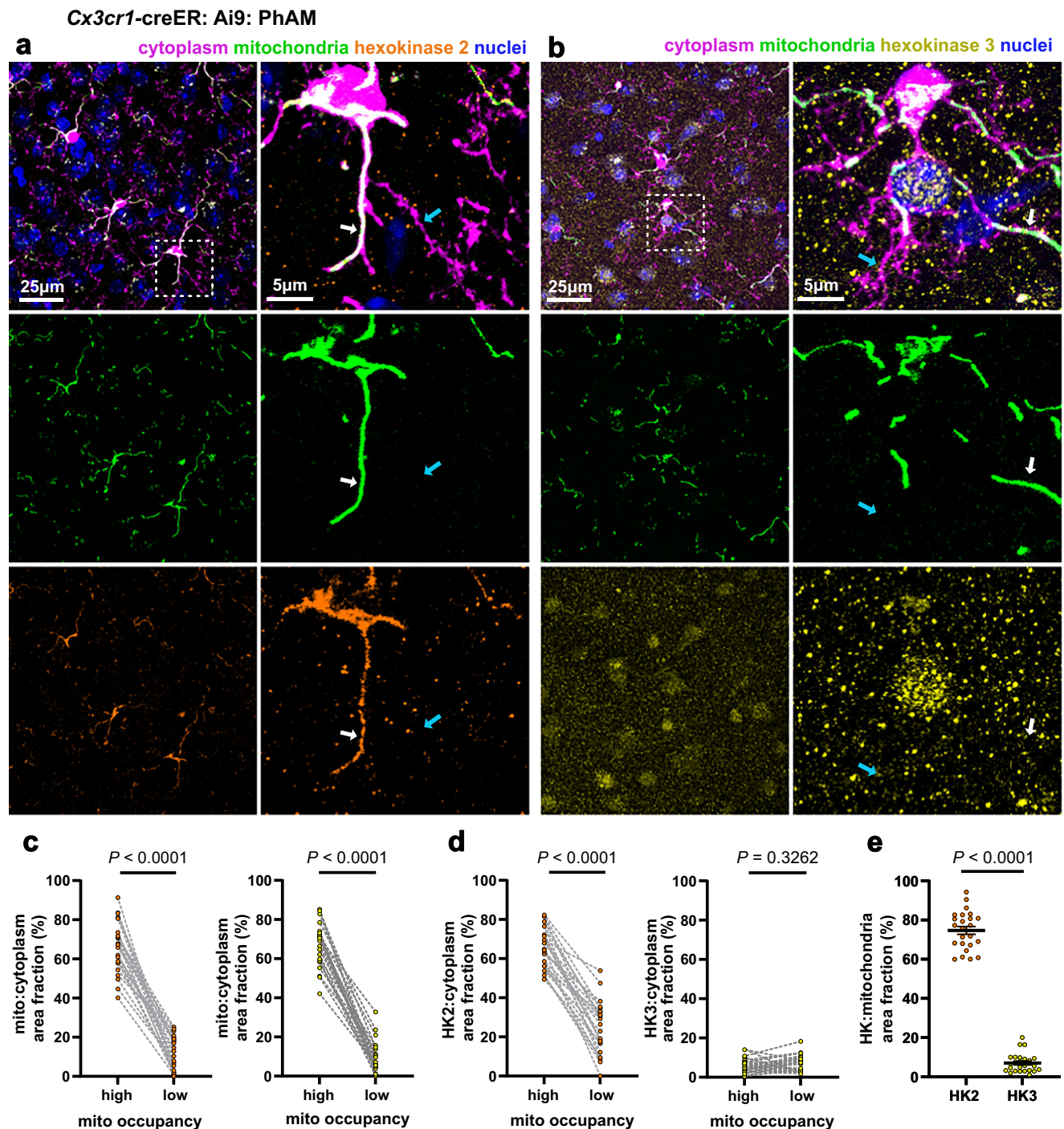
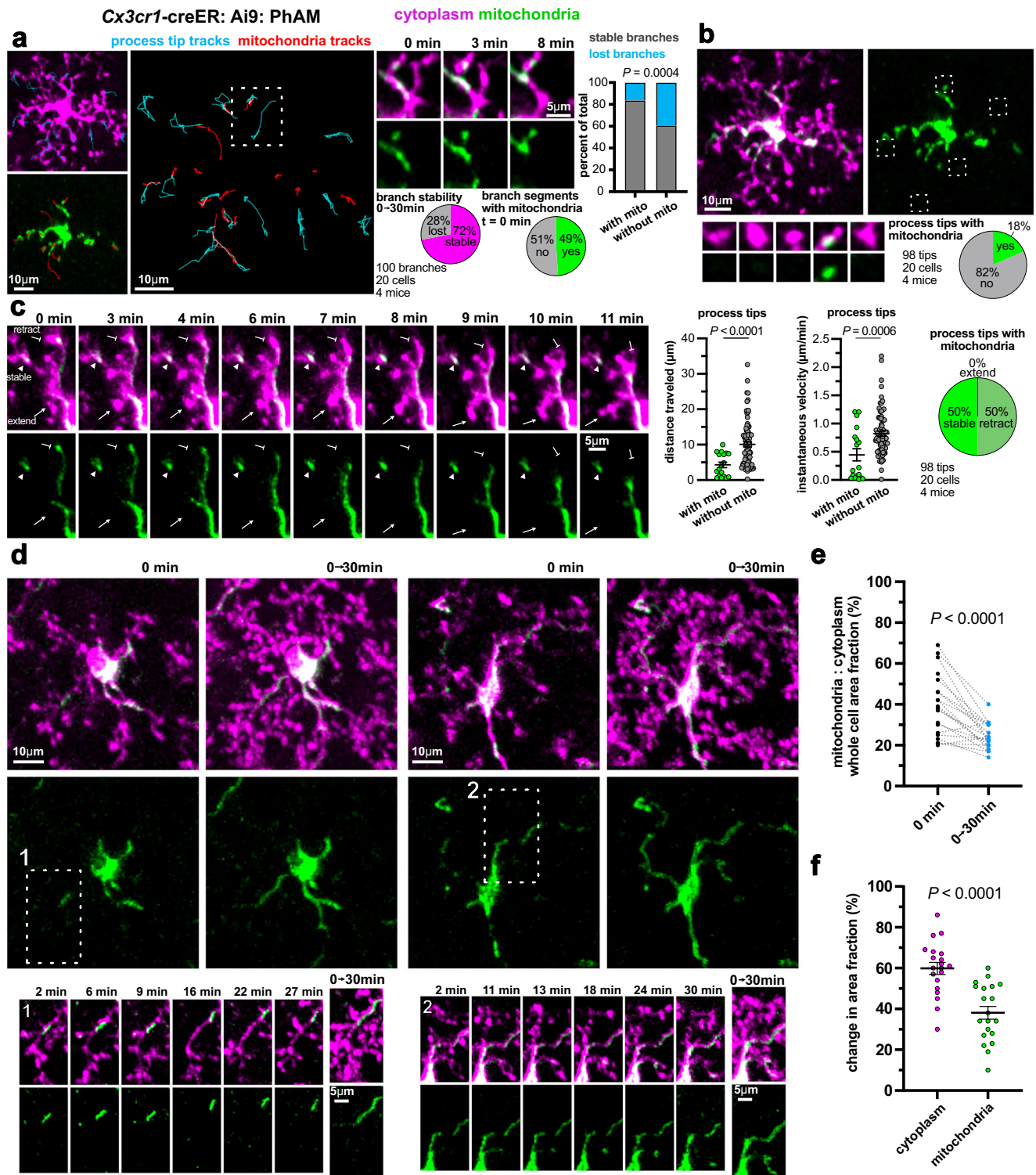


Fig. 6 | Hexokinase 2 localizes to mitochondria in microglia. **a** Images taken from the cerebral cortex of mitochondria (green) in microglia (magenta) with immunostaining for hexokinase 2 (orange). The images on the right show the boxed region from the low magnification image highlighting the asymmetric distribution of hexokinase 2 within single microglial processes and its mitochondrial association. Arrows indicate processes with low (cyan arrow) and high (white arrow) mitochondrial occupancy. **b** Images showing mitochondria (green) in microglia (magenta) immunostained for hexokinase 3 (yellow). The images on the right show the boxed region from the low magnification image highlighting the lack of hexokinase 3 labeling and little to no overlap with mitochondria. Arrows indicate processes with low (cyan arrow) and high (white arrow) mitochondrial occupancy.

c Area fraction of mitochondria within cytoplasmic ROIs for the microglial processes analyzed in the hexokinase 2 (left) and 3 (right) immunostaining conditions. **d** Area fraction of hexokinase 2 (left) and 3 (right) within cytoplasmic ROIs of processes with high or low mitochondrial occupancy. **e** Area fraction of hexokinase 2 versus 3 in mitochondrial ROIs of primary processes with high mitochondrial occupancy. For (c–e), each staining condition had $n = 96$ primary processes from 24 cells from 8 mice; **c**, **d** paired two-tailed t-tests applied; and **e** unpaired two-tailed t-test with Welch's correction applied (the line is at the mean \pm s.e.m for error bars). For (c–e) see Supplementary Figs. 3f–h and 5g–i for analyses by animal and of sex differences, respectively.



photobleaching single nuclei to trigger apoptotic death of neurons (Fig. 10a)⁵. Nuclear condensation can be observed post-2Phatal (Fig. 10a), and the neuronal corpses are cleared by microglia within 24 h^{5,6}. Therefore, 2Phatal serves as a valuable method to track mitochondria as microglia undergo the transition from recognition to early engagement engulfment of a targeted neuron. An example of individual microglia actively clearing neuronal corpses 6 h after 2Phatal can be seen alongside stable microglia that maintained their location and morphology in the parenchyma (Fig. 10a).

Stages of microglial engagement were tracked at 3, 6, and 24 h post-2Phatal and defined as (1) no engagement, (2) partial process cup

formation, (3) process engulfment, and (4) soma engulfment (Fig. 10b). At 3 h, all nuclei were partially condensed with most microglia forming a partial process cup around the nucleus. Of the microglia processes surrounding the nucleus, half were lacking mitochondria, and half had less than 50% mitochondrial presence (Fig. 10b). As the microglia engagement increased to full process or soma engulfment at 6 and 24 h, there was also an increase in mitochondrial presence within the process or soma engulfing the corpse (Fig. 10b and Supplementary Fig. 11). Fluorescent intensity measurements showed that microglia engagement gradually increased as observed in Fig. 10b (Fig. 10c and Supplementary Fig. 11). However, mitochondrial presence

Fig. 7 | Microglial branches and processes lacking mitochondria are more motile. **a** Manual tracking of microglia processes (cyan lines) and mitochondria (red lines) over 30 min suggests incongruency between the two. An example of a branch that is maintained and one that is lost with mitochondria present in the branch that is maintained. Pie charts showing the percentage of branches that are stable/lost along with the percentage of branches that contained mitochondria at the beginning of the 30 min time-series. The bar chart compares the stability of the processes that had mitochondria compared to the processes of that did not have mitochondria. (n values indicated in the figure, two-sided Fisher's exact test). **b** Percentage of microglial process tips that contained mitochondria. White dashed boxes indicate the $5 \times 5 \mu\text{m}$ ROIs that were used to determine the mitochondrial presence in the tips. **c** Time-series showing microglial process retraction, stability, or extension with corresponding presence or absence of mitochondria. Manual tracking of microglial process tips showing the total distance traveled over 30 min and instantaneous velocity in tips with or without mitochondria. Of the tips that did

have mitochondria, the pie chart shows the proportion of tips that were stable or retracting. None of the process tips that contained mitochondria extended during the 30-min time window. The n values are indicated in the figure, unpaired, two-tailed t-test (Welch's correction applied to the distance traveled graph only); the line is at the mean \pm s.e.m for error bars. **d** Temporal projections from 0 min to 30 min were used to compare microglia cytoplasmic reorganization relative to mitochondrial motility in an entire cell. The number box insets show examples across the 30 min time-series. **e** Mitochondria to cytoplasmic area fractions in temporal projections (0 \rightarrow 30 min) compared to time point 0 min, indicating that mitochondria do not move as much as the cytoplasm. **f** Mitochondria have a lower change in the area occupied relative to the cytoplasm from 0 min to 30 min. For (e, f), n = 20 cells from 4 mice; paired two-tailed t-tests; the line is at the mean \pm s.e.m for error bars. For (c, e, and f) see Supplementary Figs. 3i and 4a, b for analyses by animal; and Supplementary Fig. 6a–c for analyses of sex differences.

in the cytoplasm surrounding the nucleus was not significantly increased until 6 h after 2Phtal (Fig. 10c). Overall, very few mitochondria are found in the engulfing microglial processes at 3 h post-2Phtal, but significant mitochondrial presence became evident only at 6 h and was sustained when microglia were fully engulfing the dying cell. These findings emphasize a lack of mitochondrial presence in microglia processes during the initial stages of phagocytic engulfment of dying neurons.

Discussion

It has long been accepted that microglia have a high energy demand to perform their multifaceted, dynamic functions^{61–64}. Therefore, we hypothesized that mitochondria would reside in all parts of microglia since, even at homeostasis, microglia are in constant motion. Against our predictions, we found that mitochondria were not evenly distributed throughout microglia, nor did their motility keep up with microglial process motility. This held true in every context we investigated: general distribution of mitochondria in both mouse and human microglia (Figs. 1–3), motility/transport of mitochondria under different physiological states, and while microglia carry out surveillance, chemotaxis, and phagocytic engulfment (Figs. 7–10).

A broad look at mitochondrial distribution in neocortical microglia showed that more mitochondria resided at the cell center and decreased towards the tips of the processes consistent with previous findings from the murine retina³². These observations contradict other *in vitro* studies, as cultured microglia generally have more fragmented mitochondria spread evenly throughout the cell^{28–30}. Moreover, it generally contrasts the mitochondrial distribution seen in other neural cells in the brain. For instance, mitochondria occupy almost all the complex arborizations of neurons^{65,66} and astrocytes⁶⁷ to support metabolic and functional demands. Our analyses also found that human cortical microglia have similar mitochondrial partitioning and morphometrics to the murine microglia, namely that some microglia processes are completely devoid of mitochondria (Figs. 1 and 2), making our morphometric findings consistent across species. Together, these surprising data emphasize the importance of defining mitochondrial dynamics while microglia are maintained in their native microenvironment, as culture studies do not closely model the complex CNS environment.

In attempt to understand these stark observations of uneven partitioning of mitochondria in microglia, we first ruled out the possibility that neighboring brain structures control mitochondrial localization. From the H01 electron microscopy dataset, microglial tip proximity to blood vessels and neuronal somas did not correlate with mitochondrial localization (Fig. 4). Then, in considering the influence of the cytoskeleton, we discovered that microtubules (MTs) are likely the primary controller of mitochondrial organization in microglia since there was a significant overlap of mitochondria and MTs in the processes and some processes completely lacked both MTs and

mitochondria. (Fig. 5). This idea was supported when we discovered that mitochondria were not present in microglial processes surveilling (Fig. 7), responding to a lesion (Fig. 9), and in the initial stages of apoptotic neuron engulfment (Fig. 10). We hypothesize that MTs are not present in microglial processes in these cases. It likely takes time for the MTs to arrive and additional time for the mitochondria to get transported along them, offering an explanation as to why there is a delayed arrival of mitochondria into microglia processes performing those dynamic functions. Indeed, it has been established that surveillant microglial process motility and chemotaxis to a lesion site are dependent primarily on actin nucleation rather than microtubule polymerization^{4,58,68}. Furthermore, previous work has alluded to the need for cytoskeletal rearrangements to occur prior to successful microglial phagocytic engulfment. Namely, in the developing zebrafish, centrosome orientation and microtubule organization determine which microglia process will engulf an apoptotic neuron⁶⁹. These experiments revealed that it takes time for the centrosome to travel through the cell and enter the branch that will perform phagocytosis⁶⁹. This supports the hypothesis that the timing of mitochondrial arrival into the processes during the final stages of full engulfment is linked to actin vs microtubule cytoskeletal rearrangements occurring during the microglial injury response. Future studies are needed to explore the interplay between mitochondrial dynamics and cytoskeletal organization as microglia transition to different functional states.

Past work shows that mitochondria follow or occupy tips of regenerating axons⁷⁰, and in development mitochondria are localized to sites of forming axonal branches but not filopodium⁷¹. Also, mitochondria are at the leading edge of migrating cells^{72–74} and in the tips of filopodia in other cellular contexts⁷⁵. It's important to note these previous studies were done in cultured axons, axons of *C. elegans*, and in cancer cell lines; therefore, the temporal dynamics and cellular contexts differ from our analyses of mitochondrial partitioning in surveilling and chemotaxing microglial processes. Nevertheless, these prior studies led us to hypothesize that mitochondria would be in microglial tips undergoing surveillance and chemotaxis. However, we found there are rarely mitochondria in the tips of surveillant processes or in the microglial processes that are performing chemotaxis to the site of injury (Figs. 9 and 10). Interestingly, the surveillant process tips that do contain mitochondria, if motile, only retract but never extend (Fig. 7). Thus, microglia surprisingly orchestrate mitochondrial sub-cellular distribution and motility differently from other migratory cells or other cells undergoing extensive shape changes.

Innate immune cells undergo a metabolic shift from oxidative phosphorylation to glycolysis in response to injury to effectively host a response⁷⁶. Past work *in vitro* has shown that microglia switch metabolic profiles when exposed to inflammatory stimuli^{28–30,77}. A challenge of studying microglia in the intact brain is the inability to thoroughly investigate microglial metabolism alongside mitochondrial dynamics and how metabolism changes during surveillance, chemotaxis, and

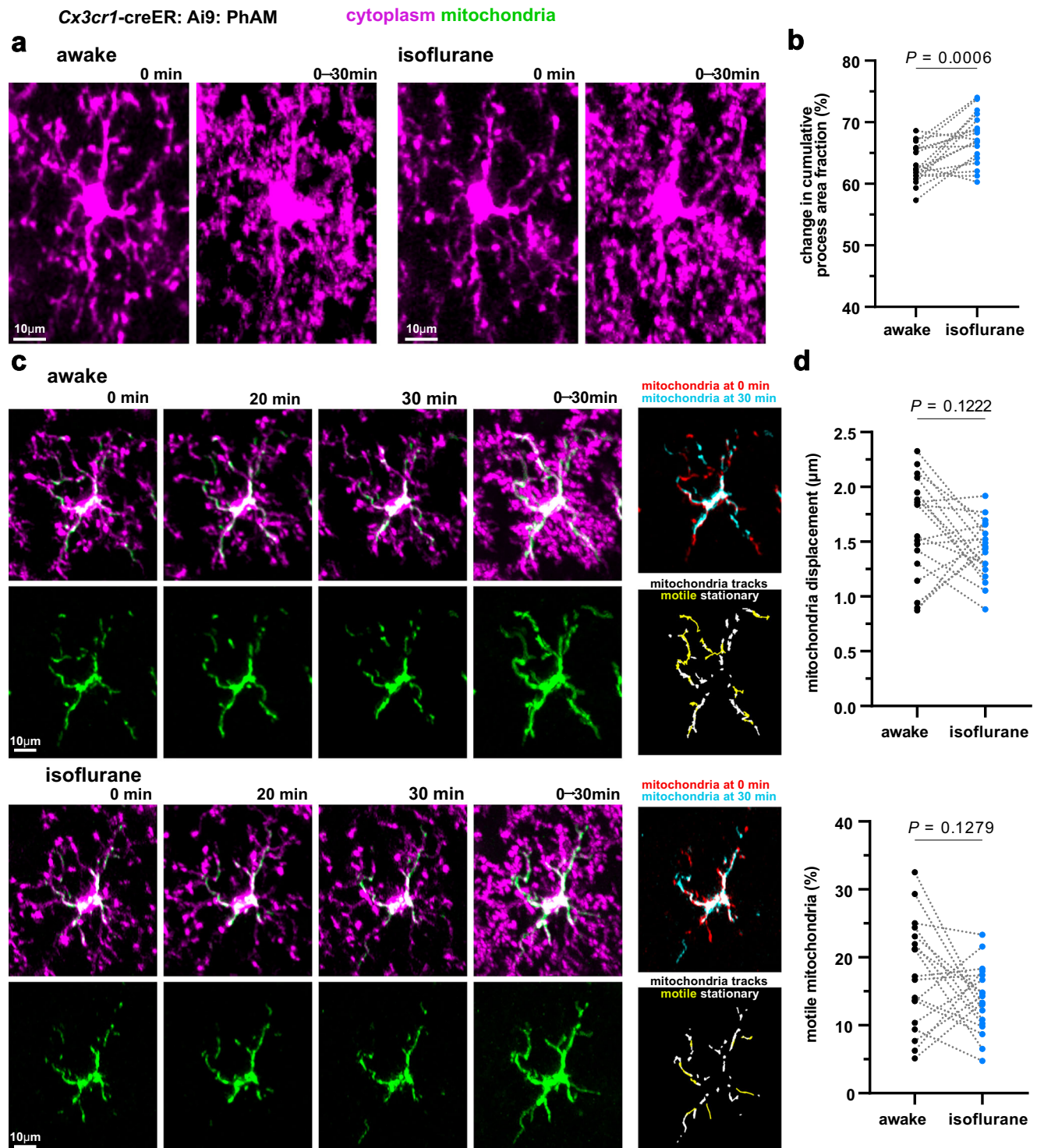


Fig. 8 | Mitochondrial motility in microglia is not altered by animal anesthesia.

a Single time point and temporal projection in vivo images of the same microglia when the animal was awake or anesthetized with isoflurane. **b** The change in cytoplasmic area fraction from the first time point to the 30 min temporal projection shows that microglial process surveillance is greater under the isoflurane condition. **c** Example time-series showing cytoplasmic and mitochondrial channels in microglia imaged in an awake mouse (top) and under isoflurane anesthesia (bottom). Temporal projections show microglial process coverage and

mitochondrial coverage over the 30 min. The images to the right show the overlap of the mitochondrial channels at 0 min and 30 min and visualization of motile mitochondria (yellow tracks). **d** Unlike the increase in process motility under isoflurane anesthesia (**b**), mitochondrial displacement (top) and the percentage of mitochondria per cell that move above a displacement threshold of 3 microns (bottom), do not significantly change in the isoflurane condition. For (**a–d**), $n = 18$ cells from 6 mice; paired, two-tailed t-tests. For (**b**, **d**) see Supplementary Figs. 4c, d and 6d–e for analyses by animal and of sex differences, respectively.

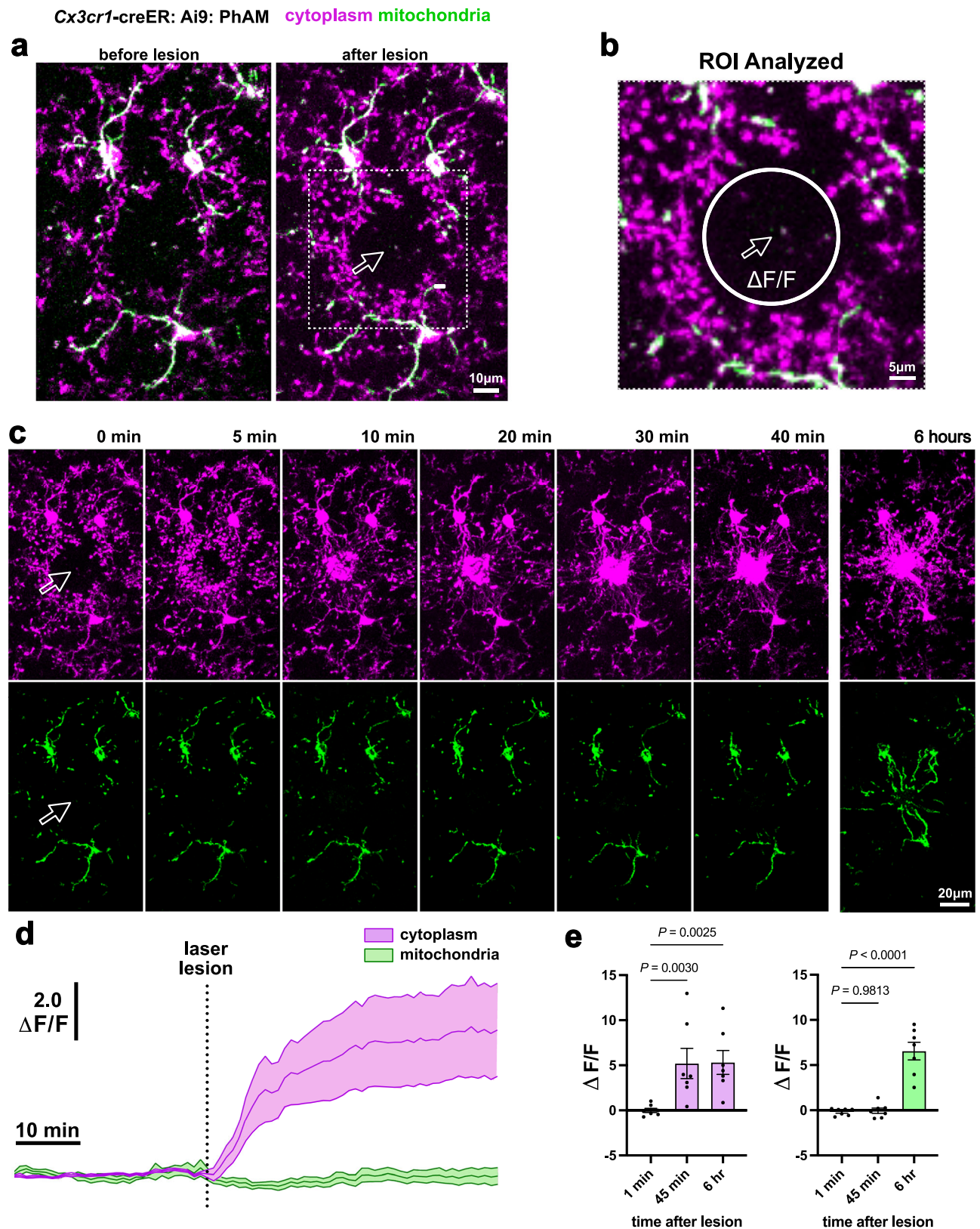


Fig. 9 | Microglial processes acutely responding to a laser lesion do not contain mitochondria. **a** A region lacking microglia was chosen for a focal laser lesion (white outlined arrow). After the lesion, a 45 min time-series was captured and at 6 h an image was taken. **b** The change in fluorescence of the microglia and mitochondrial signals before and after the lesion within the defined ROI (50×50 pixel), arrow indicates the lesion site. **c** Time-series showing the immediate chemotactic microglia process response to the site of the lesion, but little to no mitochondria response in

the same time period. **d** Fluorescence intensity measurements of the cytoplasmic and mitochondrial channels before and after the laser lesion. **e** Cytoplasmic fluorescence signals are significantly different from baseline at both 45 min and at 6 h while mitochondrial signals are not different at 45 min and but show a significant difference at 6 h after the lesion (for **(d–e)** $n = 7$ lesions from 6 mice; one-way ANOVA; mean \pm s.e.m. are represented as error bands in **(d)** or bars in **(e)**). For **(e)** see Supplementary Figs. 4e and 6f for analyses by animal and of sex differences, respectively.

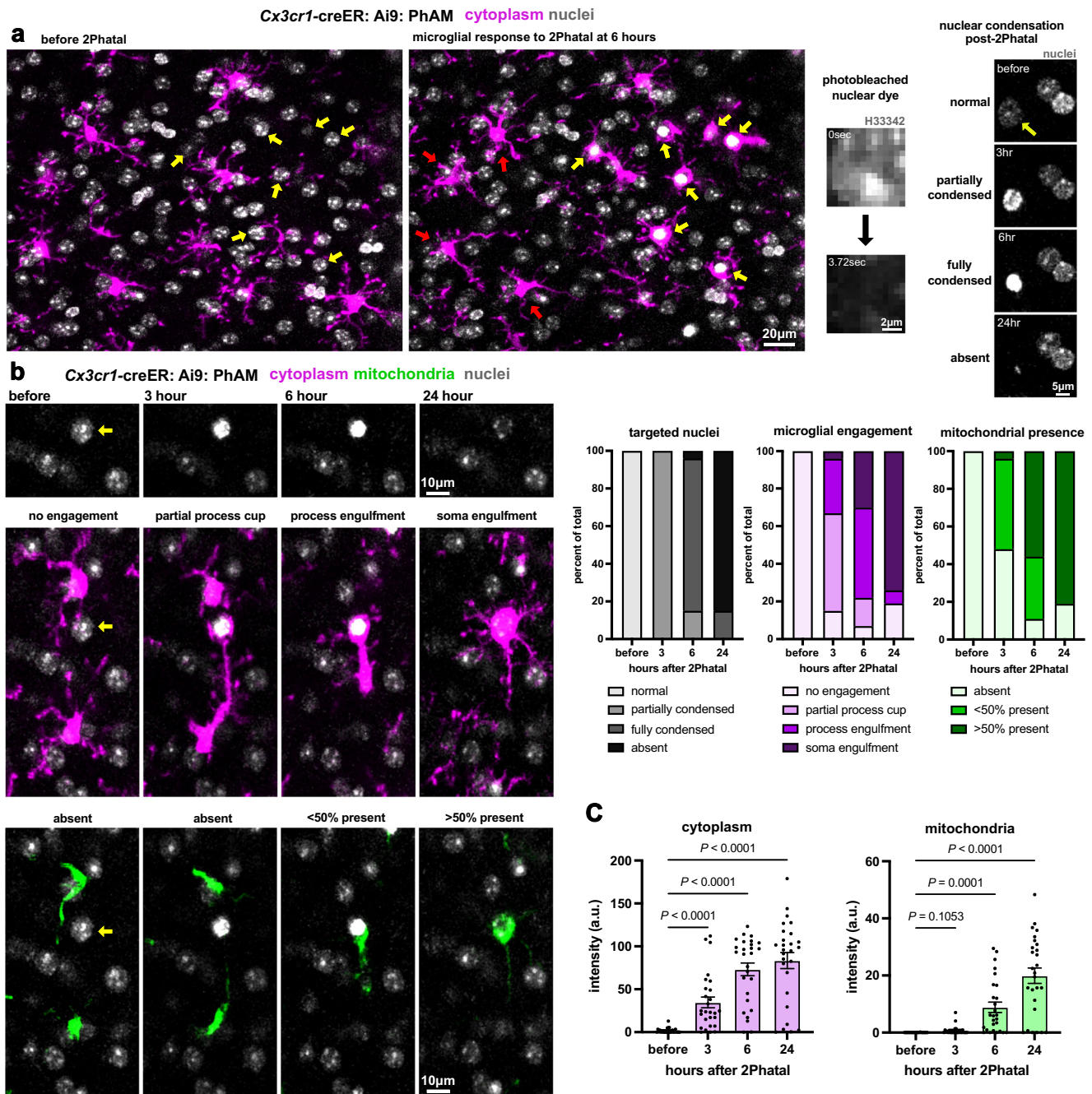


Fig. 10 | Mitochondria are delayed in their arrival to microglial processes engulfing dying neurons. **a** Labeling of nuclei (gray) and microglia (magenta) indicating cells that were targeted for 2Phtal (yellow arrows) before and 6 h after the initiation of cell death. At 6 h microglia are regularly found to engulf the condensed nuclei of the targeted cells. Nuclei were intentionally targeted on one side of the field of view, and microglia that are not engaged in phagocytosis remain ramified (red arrows). The images on the right show an example of nuclear dye photobleaching and the characteristic condensation and clearance of targeted neuronal nuclei. **b** Time-series showing the engulfment and clearance of a targeted cell (yellow arrow) revealing early cytoplasmic cup formation that lacks

mitochondrial labeling followed by full engulfment and microglial repositioning on top of the dying cell. The graphs show scoring of the nuclei (gray), cytoplasm (magenta), and mitochondrial channels surrounding targeted cells shows that while cytoplasmic signals significantly change at 3 h and remain elevated, mitochondria show increased abundance at 6 h. For **(b, c)** $n = 27$ cells from 6 mice; one-way ANOVA; mean \pm s.e.m. are represented as error bars in **(c)**. For **(c)** see Supplementary Figs. 4f and 6g, h for analyses by animal and of sex differences, respectively.

phagocytosis. One study partially circumvented this limitation by removing a metabolic protein needed for the first step of glycolysis⁵⁵, hexokinase 2 (HK2), specifically in microglia³³. They found that microglial process motility, velocity, and response to a focal lesion were all slowed in the live mouse with HK2 deleted³³. These in vivo findings were complemented with metabolic profiling in primary

cultured microglia, revealing a drop in both glycolysis and oxidative phosphorylation in the microglia lacking HK2, indicating that HK2 loss left microglia energetically depleted³³. However, when energetically challenged, microglia have been shown to be metabolically flexible switching to lipid metabolism or relying on other nutrient resources^{54,62}. Here, we revealed that HK2 is overwhelmingly localized

to microglial processes that contain mitochondria, that 75% of mitochondria are surrounded by HK2 protein, and that HK2 is highly expressed by microglia (Fig. 6) as previously reported^{33,51–54,56,57}. These data suggest that metabolic and cytoskeletal components could influence mitochondrial partitioning in microglia. There has been growing evidence that metabolic dysregulation and mitochondrial dysfunction lead to impaired phagocytic capacity of microglia, contributing to neurodegenerative disease pathology and developmental abnormalities^{31,34–36,78,79}. Future studies examining microglial bioenergetics in development, neuroinflammation, and neurodegeneration would benefit from also investigating mitochondrial morphometrics and dynamics using the approaches developed and employed here.

In summary, our findings on mitochondrial partitioning in microglia were not in line with our initial expectations. However, these data suggest that it is energetically advantageous for microglia to not contain mitochondria in all parts of the cell. In terms of process rearrangement, microglia are the most motile cells in the CNS, continually probing the microenvironment^{1,2}. Why spend the energy transporting mitochondria to all parts of microglia when their processes may only reside in a position for as little as a minute? Actin nucleation is likely sufficient to drive microglial motility, and MTs and mitochondria are only recruited when necessary. This study and other work on microglial mitochondria *in vivo*³² reveal that microglia may strategically compartmentalize resources in different parts of the cell owing to their capabilities of being metabolically flexible^{54,62,63}.

Methods

Animals

The triple transgenic mouse model used in this study, *Cx3cr1*-creER: Ai9: PHAM, was generated by breeding the following mouse lines together: *Cx3cr1*-creER (JAX strain# 020940)⁸⁰, floxed tdTomato (JAX strain# 007909)⁸¹, and PHAM (JAX #018385)³⁷. This line has conditional expression of cytoplasmic localized tdTomato (Ai9) and mitochondrial matrix localized Dendra2 (PHAM) to all CX3CR1+ cells, which are predominantly microglia in the central nervous system, but can also target border associated macrophages, therefore, no vascular associated macrophages were analyzed in this study. The other triple transgenic mouse model, *Cx3cr1*-creER: Ai9: Kaleidoscope, used in this study was generated by breeding the following mouse lines together: *Cx3cr1*-creER (JAX strain# 020940)⁸⁰, floxed tdTomato (JAX strain# 007909)⁸¹, and Kaleidoscope (JAX strain# 038639)⁸²; enabling parallel imaging of microglial cytoplasm (tdTomato, Ai9), and their mitochondria (mKate2), microtubules (eGFP), and lysosomes (BFP). Of note, the lysosomes were not analyzed for the purposes of this study. All animals used were heterozygous for creER to prevent knock out of *Cx3cr1*. To mediate Cre recombination, mice were administered an intraperitoneal (i.p) injection (0.05 mL) of tamoxifen (Sigma-Aldrich #T2859-1G) dissolved in corn oil (20 mg/mL) every other day for 5 days (total of 3 injections) at weaning. Both male and female adult mice were used at 2–6 months for the experiments⁸³. All animal procedures were approved by the Institutional Animal Care and Use Committee at Dartmouth College (protocol number: 00002158). Animal euthanasia was conducted as described in the Tissue collection section of the methods. All animals were housed in a temperature and humidity-controlled vivarium in a 12 h light/dark cycle with ad libitum access to food and water.

Surgical procedures

Cranial window surgeries were performed over the somatosensory cortex as previously described^{38,84,85}. Briefly, animals were anesthetized with an i.p. injection of ketamine (100 mg/kg) and xylazine (10 mg/kg) solution (K/X). Carprofen analgesic (50 mg/kg) was administered subcutaneously before, after, 24 h after, and 48 h after the surgery. A custom-made head plate was glued to the exposed skull, and then a craniotomy was performed to remove a circular portion of the skull

(3 × 3 mm). For 2Phatal experiments, Hoechst 33342 nuclear dye (1:175) was directly applied to the exposed brain. The brain was sealed with a no. 0 cover glass allowing for intravital imaging. Experiments were performed 3–5 weeks post-surgery to allow the surgery to heal and for inflammation to subside. However, Hoechst 33342 optimally labels nuclei 24 h after topical application to the brain; therefore, we performed the 2Phatal experiments 24 h after the cranial window surgery.

Intravital imaging

While the mouse was still anesthetized from the cranial window surgery, high resolution images were acquired on an upright confocal microscope (Leica SP8) with a 20X water immersion objective (Leica NA 1.0). The purpose of imaging immediately after the surgery is to image the brain when the cranial window is the clearest to get the best quality high resolution images which is needed for 3D reconstructions. All other imaging was performed on an upright laser-scanning 2-photon microscope (Bruker Ultima) with a 20X water immersive objective (Zeiss NA 1.0). The cytoplasmic tdTomato was excited by 552 nm and 1040 nm laser wavelength on the confocal and 2-photon, respectively. The mitochondrial Dendra2 was excited by a 488 nm and 920 nm laser wavelength on the respective microscopes. The mitochondrial mKate2, microtubule (MT) eGFP, and the Hoechst 33342 nuclear dye were excited by 1175 nm, 920 nm, and 775 nm wavelengths on the 2-photon microscope, respectively. All Z-stacks were taken over a depth of 50–60 μm with a 1.5 μm step size between stacks. The imaging depth spanned layers 1 and 2 of the somatosensory cortex. All time-series were acquired by taking a Z-stack image every 1 min for a total of 30, 45, or 60 min. For anesthetized imaging sessions isoflurane anesthesia mixed with room oxygen was delivered to the animal via the SomnoSuite, Low-Flow Anesthesia System. Initially, 3.5% isoflurane was used to induce anesthesia, then anesthesia was maintained at 1.5% isoflurane while imaging. Awake imaging experiments were performed by head fixing the mouse by the head plate in the Neurotar's Mobile HomeCage that allows the mouse to move ad libitum on an air table.

Three-dimensional segmentation and rendering from optical images

High resolution confocal images were used to segment microglial cytoplasm and their mitochondria. The image size was 2048 × 2048 pixels (pixel size 180 × 180 nm), and 1–3 positions were acquired per animal. A total of 14 microglia from 9 mice (n = 4 female and 2 male mice) were segmented. The parameter to choose the microglia to segment was that all cell compartments had to be within the Z-depth imaged. Aside from that, the cells to segment were randomly selected (1–3 cells per animal).

The Volume Annotation and Segmentation Tool (VAST Lite, version 1.4.1)⁸⁶ was used to segment the cytoplasmic (tdTomato) and mitochondrial (Dendra2) signal in 3D. Images were preprocessed in Fiji⁸⁷: the tdTomato and Dendra2 channels were split, smoothed, the look up table (LUT) changed to Grays, and converted from an 8-bit to RGB Color. The images were then imported to VAST to complete the segmentations. For each cell, first the cytoplasm was segmented to define the soma, processes, and primary process compartments. Then the mitochondrial networks were segmented and designated to the respective compartment they resided in. Lastly, with VAST we exported the following from the completed segmentations: (1) the cytoplasmic and mitochondrial volumes and (2) uncompressed TIFF images at mip level 0 (indicates the voxel resolution in X, Y, Z: 180 nm, 180 nm, 1500 nm). Both were later used in mitochondrial morphometric quantifications done in Fiji or Excel. The raw values for mitochondrial volume from the optical images were likely overestimated due to limits in axial resolution with optical fluorescence microscopy in addition to the inability to always resolve and separate single mitochondria from mitochondrial networks as mentioned in the discussion. Therefore, direct comparisons of mitochondrial volume

between the optical and EM datasets cannot be made. This does not impact other comparisons as ratio-metric or within cell comparisons are accurate.

To 3D render the microglial cytoplasm and mitochondria, MATLAB (version 24.1.0)⁸⁸ and VAST were used to export OBJ files of the cytoplasmic and mitochondrial segments at mip level 0. The OBJ files were used in 3D Slicer^{89–92} to create the 3D renderings (see examples in Fig. 1e and Supplementary Fig. 1c).

Human electron microscopy dataset analysis

To investigate mitochondria in microglia across species, we used a publicly available human electron microscopy (EM) dataset (H01) available online at <http://h01-release.storage.googleapis.com/landing.html>⁴². This dataset provides a complete cellular and vascular reconstruction of 1 cubic millimeter of the temporal cortex, the largest reconstruction of the human brain to date⁴². The brain tissue was donated from a 45-year-old female who underwent an epilepsy-related resection surgery⁴². To access and resect the epileptic focus, a section of the brain tissue above it was removed— a portion of which constitutes the H01 dataset⁴².

The tissue was prepared as described⁴², sectioned at ~30 nm thickness, and imaged using multibeam scanning electron microscopy with a resolution of $4 \times 4 \text{ nm}^2$. This group automated segmentation of cells and vasculature, which can be viewed in Neuroglancer⁴². We distinguished microglia from OPCs by their nuclear ultrastructure and cell cytoplasmic morphology⁴³. Using Neuroglancer, we chose 6 microglia from cortical layer 5 to further segment their mitochondria. We used VAST⁸⁶ to open the H01 dataset, import the coordinates of our cells of interest taken from Neuroglancer, and fill the microglia cytoplasm that had already been automatically segmented⁴². We further segmented other microglial compartments, including the soma, processes, primary processes, nucleus, and mitochondria. Mitochondria were designated to their respective compartment. Similar to the fluorescent segments, we used VAST to export the following from the specific bounding area of the EM segmentations: (1) the cytoplasmic, nuclear, and mitochondrial volumes and (2) uncompressed TIFF images at mip level 4 (X, Y, Z: 128 nm, 128 nm, 132 nm). A higher mip level lowered the resolution such that images could be exported in a timely manner. These exports were later used for mitochondrial morphometric quantifications done in Fiji or Excel.

To determine microglia process tip proximity to vasculature, vasculature and microglia segmentations were opened in Neuroglancer. For each microglia primary process, 2 tips were selected, and coordinates were recorded. At each tip, the nearest blood vessel was identified using 2D visualization of EM data simultaneously in the xy, xz, and yz planes, and the coordinates were recorded. The recorded coordinates were used to calculate the distance between each microglia tip and the nearest blood vessel. To determine the mitochondrial volume fraction at each tip, segmentations made in VAST of microglia process cytoplasm and mitochondria were exported as a tiff for a $20 \mu\text{m} \times 20 \mu\text{m} \times 20 \mu\text{m}$ region centered at each microglia tip. In Fiji, microglial cytoplasm and mitochondria area were calculated from maximum projections.

To determine microglial process tip proximity to neighboring neurons, the nearest neighboring neuron soma was identified using 2D visualization of EM data simultaneously in the xy, xz, and yz planes in Neuroglancer. Some microglia somas (4/6) directly contacted neurons. For each identified neuron, coordinates were recorded in the center of the neuron soma. For each microglia, coordinates were recorded in the center of the soma and at process tips as described above. Coordinates were used to calculate distances between neuron somas and microglia somas or tips. Microglia mitochondria volume fractions were determined as described above. Visualizations of other cells contacting microglia were made in Neuroglancer.

Mitochondrial morphometric analysis

Morphometrics in this study encompass mitochondrial content, shape, and subcellular distribution. Starting with content, all volume exports from the 3D segmentations were used to determine the mitochondrial to cytoplasmic volume fraction (%) and the total or average mitochondrial volume (μm^3) in the whole microglia and/or by microglial compartment (soma and processes). Additionally, mitochondrial network number and the number of individual mitochondria were manually counted while segmenting the optical (mouse) and EM (human) datasets, respectively. For the optical dataset, if a mitochondrial network spanned more than one compartment, its volume was split to represent the compartment it resided in, but it was counted as one network. For the EM dataset, if a mitochondrion spanned more than one compartment, it was assigned to the one it most occupied.

From the optical segmentations, mitochondrial shape was determined by circularity and aspect ratio: two different calculations to determine how circular or elongated an object is. A value equal to 1.0, from both circularity ($4\pi(\text{area}/\text{perimeter}^2)$) and aspect ratio (width/length), represents an object that is a perfect circle. Therefore, as the value moves further from 1.0, the object becomes more elongated. To quantify the mitochondrial shape, mitochondrial segments from each microglia were opened in Fiji, a maximum intensity projection was made, default threshold applied, then the “Analyze Particles” command was used to automatically calculate circularity and aspect ratio from the shape descriptors. Circularity and aspect ratio consider different features of the object. Using both methods ensures a thorough analysis, as one calculation might not detect a shape difference, while the other does.

Multiple analyses were used to dissect the subcellular distribution of mitochondria in microglia. First, a Sholl analysis was done on the cytoplasmic and mitochondrial segments (from optical and EM datasets) separately. Sholl is used on cells with a branched morphology to determine the complexity of the branching. It does this by counting the number of intersections that branches make on evenly spaced concentric circles that radiated out from the cell center. With Sholl, we wanted to determine how mitochondria radiate from the cell center relative to the microglial branching complexity. To perform Sholl, maximum intensity projections were made from the cytoplasmic and mitochondrial segments in Fiji, a default threshold was applied, a straight line was drawn from the cell center to the edge of the image, and the “Neuroanatomy” plugin was used to execute Sholl. Sholl parameters for the optical dataset were set to $1 \mu\text{m}$ for the starting radius and step size with a $70 \mu\text{m}$ ending radius. Given the increased spatial resolution of the EM dataset, we used the following Sholl parameters: $0.5 \mu\text{m}$ for the starting radius and step size with an $80 \mu\text{m}$ ending radius. Results were graphed as number of intersections against the distance from the cell center. Of note, to exclude contributions from the soma, radii 1–8 μm were excluded from the Sholl graphs (Figs. 1 and 2) since the average soma radius of microglia is around $8 \mu\text{m}$ in the optical and EM datasets.

The second set of analyses determined the subcellular distribution of mitochondria along the length of individual primary processes in 10% bins. To measure the primary process lengths, the optical 3D segments (from the cell soma and the primary process cytoplasm and mitochondria) were first maximum intensity projected and merged into one image in Fiji. In the merged image, only the cytoplasm and soma channels were made visible. The mitochondrial channel was off to ensure the researcher was blind to the mitochondria location along the primary branch length. Next, a 5-pixel segmented line tool was used to trace the longest branch in the primary process from soma end to tip end, such that the shortest possible path was traced. Then, the “Plot Profile” command was executed in reference to the mitochondrial channel, which provided the primary process length (μm) and

information (from gray value) on where mitochondria specifically reside along that length. To interpret this information, the length of all the primary processes was normalized to each other by considering the length as 0–100% (soma = 0% and tip of process = 100%) and quantifying the mitochondrial occupancy in 10% bins along the length of the primary process. This method was a more thorough and used to confirm findings from the Sholl analysis.

The third set of analyses further described mitochondrial subcellular distribution in primary processes by scatter plotting the mitochondrial volume in each primary process (μm^3) by the primary process length (μm) with both the optical and EM datasets. The primary process lengths of the human EM microglia were measured with plot profile as described above. Primary process length, not cytoplasmic volume, was used in these analyses to distinguish long processes from short processes. Cytoplasmic volume was misleading because some short processes had greater volume than longer and thinner processes.

Lastly, Excel was used to perform a k-means cluster ($k = 2$) using the mitochondrial volume per primary process. This unbiased clustering approach defined two groups that contained either high mitochondrial volume ($>67.1 \mu\text{m}^3$) or low mitochondrial volume ($<67.1 \mu\text{m}^3$). Within those 2 groups we determined the circularity and aspect ratio of the individual mitochondrial networks in each primary process (excluding the primary processes lacking mitochondria). The goal of this analysis was to determine if mitochondrial shape in a microglia process differs depending on the volume of mitochondria occupying that process. We used the optical mouse dataset for this analysis given the abundance of primary processes analyzed.

Microtubule (MT) and mitochondrial distribution

The *Cx3cr1-creER; Ai9*: Kaleidoscope mouse model was used to determine MT and mitochondrial distribution in microglia. Images acquired from the 2-photon microscope were 1024×1024 pixels (pixel size of 213×213 nm), and 2 positions were acquired per animal ($n = 2$ female and 3 male mice). In Fiji, the images were smoothed then 3–4 microglia/animal were selected for analysis and cropped with a $75 \times 75 \mu\text{m}$ ROI. A $13.5 \mu\text{m}$ maximum intensity projection was made for each cell with the soma in the center of each Z depth projected. From the cropped microglia each channel was automatically thresholded: cytoplasm/tdTom was default thresholded, and the MT/eGFP and mitochondrial/mKate2 channels were Max Entropy thresholded. Then, the area fraction of each thresholded channel was acquired to calculate the MT:cytoplasm and mitochondria:cytoplasm area fractions within each microglia ($n = 19$ microglia from 5 mice, 2 female and 3 male).

Next, 12 of the microglia selected above were used to analyze the presence of MTs relative to mitochondrial presence. In each cell, 2 processes with and 2 processes without mitochondria were selected with the researcher blind to the MT channel. Then, $5 \times 5 \mu\text{m}$ ROIs were overlaid on the processes selected, and the MT channel was turned on to quantify the percentage of processes containing MTs.

Mitochondrial presence during microglial surveillance

To determine mitochondrial presence during microglial surveillance, animals were imaged under isoflurane anesthesia 3–5 weeks after the cranial window surgery (see *Surgical Procedures* and *Intravital Imaging*). A 30 min time-series was captured from 4 mice ($n = 2$ female and 2 male mice). In Fiji, the time-series was 3D Drift Corrected based on the tdTomato channel, then 25 microglia were selected also using the tdTomato channel. Each microglial cell was cropped, smoothed, and then maximum intensity projected from the 5 slices above and 5 slices below the center of the microglial soma. Then, branches (3–6 per cell) and process tips (3–6 per cell) were selected (using the tdTomato channel) from each microglia and the following analyses were performed.

We defined the branches as “stable”, present at 0 min and 30 min, or “lost”, branch was present at 0 min but gone at 30 min. Stable branches were considered less motile than the lost branches. With this we determined the percentage of branches that were stable or lost. To confirm that the branches selected had no difference in mitochondrial occupancy at time point 0 min, we determined the percentage of branches that contained and did not contain mitochondria. Then, we determined the percentage of branches containing mitochondria in the stable branches vs. the lost branches. Given that much motility occurs at the tips of the processes we overlaid a $5 \times 5 \mu\text{m}^2$ region of interest (ROI) around the tip's center and determined the percentage of tips that contained or did not contain mitochondria.

Next, we quantified the area covered by the cytoplasmic and mitochondrial signal across the 30 min time-series by temporally projecting all the 30 images together (designated as 0→30 min). We visualized process and mitochondrial motility from manual tracks made in the Fiji's TrackMate plugin. An increase in area fraction indicates motility, therefore, we aimed to quantify the motility by these methods to compare microglial process and mitochondrial motility during surveillance. Each cropped cell was further processed in Fiji: the cytoplasmic and mitochondrial channels were split, bleach corrected, “Li” thresholded to make a binary image with minimal background signal, and finally temporally projected. From this, area fraction from the cytoplasmic and mitochondrial channels was determined from the 0 min image and the temporal projection 0→30 min. We determined the percent of mitochondrial to cytoplasmic area fraction, and the percent change in area fraction for each signal separately.

Next, we quantified the instantaneous velocity for the tips of the processes that were defined in the ROIs described above. Each process tip was manually tracked using the “Manual Tracking” plugin in Fiji while blinded to the Dendra2/mitochondrial channel. The process tips were tracked for the whole duration of the 30 min time-series or, in case of retraction, until they merged into the soma or parent process. The processes with mitochondria were later qualitatively classified as stable, extending, or retracting.

Awake to isoflurane anesthetized imaging and analysis

Awake to anesthetized imaging was performed 3–5 weeks after the cranial window surgery (see *Surgical Procedures* and *Intravital Imaging*). First, the animal was acclimated to the Neurotar Mobile HomeCage for 30 min, then a 30 min time-series was captured. Next, the same animal was removed from the awake imaging set-up and anesthetized. We allowed the mouse to acclimate to the anesthesia for 30 min before locating the same position that was imaged during wakefulness. Then, a 30 min time-series was captured. Therefore, two 30 min time-series were acquired from the same animal in the same position: first during wakefulness and then during anesthesia allowing us to compare the same microglia and their mitochondria under different arousal states ($n = 6$ mice, 3 female and 3 male).

For analyzing the mitochondria and processes' dynamics in awake and isoflurane anesthetized conditions, first, the Z-stacks were registered to correct for the Z-drift with reference to the cytoplasmic channel. The cells to be analyzed were randomly selected with reference only to the first time point and the analyzer was blinded to the experimental condition. The cells were cropped, smoothed, and used to create maximum intensity Z-projections which were later thresholded similarly for the mitochondria and cytoplasmic channel. To measure the processes' dynamics, Z-projections of the first and last time points as well as of all the time points along the 30 min time-series were created for the cytoplasmic channel. Area fraction in the cropped region was measured for the first time point as well as for the temporal projections and the change in area fraction between the two was calculated.

Mitochondria motility analysis was done only for the mitochondria in the processes of the selected cells, and mitochondria present in

the soma or other cells in the environment were cleared out. The thresholded images were then run in TrackMate³³ with the following settings: the LoG detector was selected, and the estimated object diameter was set at 3, quality threshold at 1, and sub-pixel localization was checked; the simple LAP tracker was selected, and the linking and gap-closing max distance was set at 3 microns, and gap-closing max frame gap at 2. The tracks with less than 5 spots were excluded and displacement was collected for each of the automatically tracked mitochondria networks. To correct for any remaining drift caused by imaging and sample motion artifacts, first, the mitochondria track that traveled the smallest distance along the 30 min time-series was identified. It was assumed that any displacement collected from this track was due to drift and therefore all the other displacement values were corrected accordingly based on this track. All the above steps were kept consistent for both awake and isoflurane conditions. Lastly, all the mitochondria displacement values of all the tracks analyzed in both conditions were combined to calculate the mean and standard deviation. Their sum (rounded up to 3 microns) was determined to be the displacement threshold above which the mitochondria tracks were considered motile.

Laser lesion imaging and analysis

The laser lesion experiment was performed in awake animals using the Neurotar Mobile HomeCage 3–5 weeks after the cranial window surgery (see *Surgical Procedures and Intravital Imaging*). The laser power was increased to ~75 mW for the lesion. The high laser power used for the lesion causes cell rupture and spillage of ATP into the parenchyma³. ATP then triggers a chemotactic response from microglia via the transmembrane purinergic P2Y12 receptor⁹⁴. This method of applying focal tissue damage serves as a model of acute inflammatory response by microglia. Before the lesion was induced a 30 min time-series was acquired to capture baseline surveillance. In the same position, a laser lesion was induced in an 8 × 8-pixel ROI in an area with little to no fluorescent signal, then immediately after the lesion a 45 min time-series was captured. This allowed us to observe the microglial transition from baseline surveillance to rapid chemotactic response to the lesion and assess the mitochondrial positioning and motility throughout this process. Additionally, the same position was imaged at 1 and 6 h after the lesion to observe the progression of mitochondrial dynamics as microglia work to clear the debris. The same position was identified at each time point using the vascular morphology and cellular patterning. One to two laser lesions were induced in each animal (n = 6 mice, 3 female and 3 male).

To determine when microglial processes and mitochondria arrive to the laser lesion, the change in fluorescence over time was quantified in the region surrounding the lesioned area. To do this the 30 min and 45 min time-series were preprocessed as follows: a maximum intensity projection was made, the tdTomato and Dendra2 channels were each bleach corrected, then the projection was corrected for 3D drift, referring to the Dendra2 channel, the tdTomato and Dendra2 channels were split, then the lesion location was identified. Next, the “Li” threshold was applied to the projections to create a binary image stack of each channel and remove background signal. Then, a 50 × 50-pixel ROI was centered around lesion site ROI (Fig. 9b), and the “Time Series Analyzer V3” FIJI plugin was used to quantify the average fluorescent intensity around in the donut ROI over time. The average fluorescent intensities across the 30 min times-series were averaged for each position and channel (tdTomato and Dendra2) imaged. This average served as the baseline fluorescence for the position, and it was used to calculate the change in fluorescent intensity minute by minute for the 30 min before and 45 min after the lesion was induced. The change in fluorescent intensity was also quantified from a single 6 h time point to determine the possible progression of mitochondrial arrival to the lesion site.

2Phatal imaging and analysis

Targeted two-photon chemical apoptotic ablation (2Phatal) experiments were performed in awake animals using the Neurotar Mobile HomeCage 24 h after the cranial window surgery (see *Surgical Procedures and Intravital Imaging*). 2Phatal enabled us to trigger apoptotic death of single neurons⁵ in layer 2 of the somatosensory cortex. We observed the microglia mitochondrial response to this non-inflammatory injury^{7–9} as a single microglia recognized the apoptotic neuron and initiated phagocytosis of the neuronal corpse^{5,6}. Neuronal nuclei were identified by their granular morphology and large size⁵. 2Phatal was induced as previously described^{5,84}. Briefly, an 8 × 8-pixel ROI was placed over the Hoechst 33342 labeled neuronal nucleus, the dwell time was increased to 100 μs, the laser intensity was increased, and then the nuclear dye was laser ablated for 3.2 s. This damages the DNA and triggers apoptosis⁵. One position per animal was captured and within each position, 1–8 neuronal nuclei were targeted (n = 6 mice, 4 female and 2 male). Images were taken before, 3 h, 6 h, and 24 h after 2Phatal. The same position was identified at each time point using the vascular morphology and nuclear patterning. This is a valuable non-inflammatory cell death method that enables visualization of how the mitochondrial dynamics interplay with the microglial process dynamics when clearing a single neuron.

First, we qualitatively assessed the nuclear condensation, microglial engagement, and mitochondrial presence at each time point imaged (before, 3 h, 6 h, and 24 h). Nuclear condensation was defined as either normal, partially condensed, fully condensed, or absent. Microglial engagement was defined as no engagement, partial process cup, process engulfment, or soma engulfment. Mitochondrial presence was defined as absent, <50% present, or >50% present. These scorings of engagements were individually graphed to show the percentage of total cells presenting the specific nuclear, cytoplasmic, and mitochondrial phenotypes before and after 2Phatal.

For a quantitative assessment of the microglial cytoplasmic and mitochondrial response to clearing an apoptotic neuron, we determined the average fluorescent intensity at each time point (before, 3 h, 6 h, and 24 h) imaged post-2Phatal. To perform this analysis in FIJI, a 20 × 20 μm² circular ROI was centered the 2Phatal targeted nuclei to produce a cropped image for each nucleus at each time point. From the cropped images, the channels (tdTomato and Dendra2) were split, and a default threshold was applied to each image. Then, a 20 × 20 μm² circular ROI was overlaid on each image and the mean gray value was effectively quantified around the immediate vicinity of the target nucleus across all time points and in both the cytoplasmic and mitochondrial channels.

Tissue collection, immunohistochemistry, and analysis

At P125–158 and 5–6 weeks after the cranial window surgery, mice were anesthetized with K/X and transcardially perfused with 4% paraformaldehyde solution diluted in 1X PBS. Brains were fixed for 24 h in 4% paraformaldehyde and then moved to 1X PBS for long term storage. Brains were sectioned at 75 μm thickness with a vibratome and cryopreserved at –20 °C.

For immunohistochemistry, the following materials were used: primary antibodies included rabbit anti-TOMM20 (1:200, Abcam, #ab78547), rabbit anti-hexokinase 2 (1:100, Abcam, #ab209847), and rabbit anti-hexokinase 3 (1:100, Proteintech, #13333-1-AP); the secondary antibody was donkey anti-rabbit 647 (1:500, Jackson ImmunoResearch Laboratories Inc., #711-605-152); Hoechst 33342 nuclear dye diluted in 0.3% Triton X-100 in 1X PBS (1:2000, Thermo Fisher Scientific, #H3570); and Prolong Diamond Mountant (P36970). Primary and secondary antibodies were diluted in 0.3% Triton X-100 and 1% Bovine Albumin Serum in 1X PBS. For the immunostain procedure, free floating brain sections were first incubated in primary antibody solution overnight, then incubated in the secondary antibody solution

for 2 h, and lastly the nuclear dye solution was applied for 30 minutes. Before and after each step of the procedure, the slices were washed with 1X PBS, and throughout the procedure incubations and washes occurred on a shaker at RT. The sections were mounted and stored at 4 degrees Celsius until imaged on a confocal microscope with a 63X oil immersion objective (Leica NA 1.4). Each section was imaged in the somatosensory cortex, spanning layers 1–2, region. All fixed tissue analysis was performed in FIJI.

TOMM20 staining was performed to determine the recombination efficiency of Dendra2. Four microglia per animal were analyzed (n = 4 mice, 2 female and 2 male). Five TOMM20 labeled spots within the cell cytoplasm were randomly selected per cell while being blinded to the Dendra2 channel (total of 80 spots). Each of the spots was later qualitatively assessed to determine the overlap rate of the two mitochondrial labels, Dendra2 and TOMM20.

For analysis of hexokinase distribution the following was done for HK2 and HK3 immunostains. Three microglia from each animal were analyzed (n = 8 mice, 5 female and 3 male). For each microglia analyzed, 2 processes with high and 2 processes with low mitochondrial occupancy were selected with only the cytoplasmic (tdTomato) and mitochondrial (Dendra2) channels; the researcher was blind to the hexokinase 2 and 3 channels. For each process, a maximum intensity projection of two Z slices was “default” thresholded for the cytoplasmic channel, and “moments” thresholded for the mitochondrial and hexokinase channels. Then, an 8.50 × 5.50 pixel ROI was used to crop the selected process (while blind to the hexokinase channels). Next, the “Analyze Particles” command was used to automatically generate ROIs of the cytoplasm and mitochondria within the cropped ROI. Lastly, the area fraction of hexokinase signal within the cytoplasmic and mitochondrial ROIs was acquired.

Statistical analysis

All statistical analyses were performed using GraphPad Prism (version 10.3.0) or Excel. No statistical methods were used to predetermine sample size, and all data was assumed to have a normal distribution. For t-tests, variance was tested and if significant then Welch’s correction was applied and noted in the figure legend. Sample sizes were based on those reported in previous publications. Statistical tests, cell numbers, and animal numbers are indicated in the figure legends for each experiment. The parameters to select the cells analyzed in this study were based on the quality of the images and that all cell compartments were within the imaged Z depth. The cells for the motility analyses were randomly selected with reference to the first time point of the time-series, and the data was blinded for awake and isoflurane anesthetized conditions. The cells analyzed from the EM dataset were selected based on the microglial identification criteria. Throughout the study, the analyzer only referred to the cytoplasmic channel, and not the mitochondrial channel, when defining ROIs to prevent bias to on the regions selected. For applicable datasets, data was analyzed by animal and sex differences were determined which are detailed in Supplementary Figs. 3–6. No animals were excluded from the statistical analysis.

Reporting summary

Further information on research design is available in the Nature Portfolio Reporting Summary linked to this article.

Data availability

All the analyzed data are represented within the manuscript and all the other data are available from the corresponding author upon unrestricted request. Source data are provided with this paper.

References

- Nimmerjahn, A., Kirchhoff, F. & Helmchen, F. Resting microglial cells are highly dynamic surveillants of brain parenchyma in vivo. *Science* **308**, 1314–1318 (2005).
- Paolicelli, R. C. et al. Microglia states and nomenclature: a field at its crossroads. *Neuron* **110**, 3458–3483 (2022).
- Davalos, D. et al. ATP mediates rapid microglial response to local brain injury in vivo. *Nat. Neurosci.* **8**, 752–758 (2005).
- Hines, D. J., Hines, R. M., Mulligan, S. J. & Macvicar, B. A. Microglia processes block the spread of damage in the brain and require functional chloride channels. *Glia* **57**, 1610–1618 (2009).
- Hill, R. A., Damisah, E. C., Chen, F., Kwan, A. C. & Grutzendler, J. Targeted two-photon chemical apoptotic ablation of defined cell types in vivo. *Nat. Commun.* **8**, 15837 (2017).
- Damisah, E. C. et al. Astrocytes and microglia play orchestrated roles and respect phagocytic territories during neuronal corpse removal in vivo. *Sci. Adv.* **6**, eaba3239 (2020).
- Henson, P. M., Bratton, D. L. & Fadok, V. A. Apoptotic cell removal. *Curr. Biol.* **11**, R795–R805 (2001).
- Takahashi, K., Rochford, C. D. P. & Neumann, H. Clearance of apoptotic neurons without inflammation by microglial triggering receptor expressed on myeloid cells-2. *J. Exp. Med.* **201**, 647–657 (2005).
- Kawabori, M. & Yenari, M. A. The role of the microglia in acute CNS injury. *Metab. Brain Dis.* **30**, 381–392 (2015).
- Picard, M. & Shirihai, O. S. Mitochondrial signal transduction. *Cell Metab.* **34**, 1620–1653 (2022).
- Monzel, A. S., Enríquez, J. A. & Picard, M. Multifaceted mitochondria: moving mitochondrial science beyond function and dysfunction. *Nat. Metab.* **5**, 546–562 (2023).
- Liesa, M. & Shirihai, O. S. Mitochondrial dynamics in the regulation of nutrient utilization and energy expenditure. *Cell Metab.* **17**, 491–506 (2013).
- Fung, T. S., Chakrabarti, R. & Higgs, H. N. The multiple links between actin and mitochondria. *Nat. Rev. Mol. Cell Biol.* **24**, 651–667 (2023).
- Twig, G. et al. Biophysical properties of mitochondrial fusion events in pancreatic β -cells and cardiac cells unravel potential control mechanisms of its selectivity. *Am. J. Physiol. Cell Physiol.* **299**, C477–C487 (2010).
- Marik, C., Felts, P. A., Bauer, J., Lassmann, H. & Smith, K. J. Lesion genesis in a subset of patients with multiple sclerosis: a role for innate immunity?. *Brain J. Neurol.* **130**, 2800–2815 (2007).
- Streit, W. J., Braak, H., Xue, Q.-S. & Bechmann, I. Dystrophic (senescent) rather than activated microglial cells are associated with tau pathology and likely precede neurodegeneration in Alzheimer’s disease. *Acta Neuropathol.* **118**, 475–485 (2009).
- Damani, M. R. et al. Age-related alterations in the dynamic behavior of microglia. *Aging Cell* **10**, 263–276 (2011).
- Safaiyan, S. et al. Age-related myelin degradation burdens the clearance function of microglia during aging. *Nat. Neurosci.* **19**, 995–998 (2016).
- Mecca, C., Giambanco, I., Donato, R. & Arcuri, C. Microglia and aging: the role of the TREM2–DAP12 and CX3CL1–CX3CR1 Axes. *Int. J. Mol. Sci.* **19**, 318 (2018).
- Hill, R. A., Li, A. M. & Grutzendler, J. Lifelong cortical myelin plasticity and age-related degeneration in the live mammalian brain. *Nat. Neurosci.* **21**, 683–695 (2018).
- Angelova, D. M. & Brown, D. R. Microglia and the aging brain: are senescent microglia the key to neurodegeneration?. *J. Neurochem.* **151**, 676–688 (2019).
- Leng, F. & Edison, P. Neuroinflammation and microglial activation in Alzheimer disease: where do we go from here?. *Nat. Rev. Neurol.* **17**, 157–172 (2021).
- Choi, S., Guo, L. & Cordeiro, M. F. Retinal and Brain Microglia in Multiple Sclerosis and Neurodegeneration. *Cells* **10**, 1507 (2021).
- Malvaso, A. et al. Microglial senescence and activation in healthy aging and Alzheimer’s disease: systematic review and neuropathological scoring. *Cells* **12**, 2824 (2023).

25. McAvoy, K. & Kawamata, H. Glial mitochondrial function and dysfunction in health and neurodegeneration. *Mol. Cell. Neurosci.* **101**, 103417 (2019).
26. Li, Y., Xia, X., Wang, Y. & Zheng, J. C. Mitochondrial dysfunction in microglia: a novel perspective for pathogenesis of Alzheimer's disease. *J. Neuroinflamm.* **19**, 248 (2022).
27. Ulland, T. K. et al. TREM2 maintains microglial metabolic fitness in Alzheimer's disease. *Cell* **170**, 649–663.e13 (2017).
28. Kato, M. et al. Polymorphic regulation of mitochondrial fission and fusion modifies phenotypes of microglia in neuroinflammation. *Sci. Rep.* **7**, 4942 (2017).
29. Nair, S. et al. Lipopolysaccharide-induced alteration of mitochondrial morphology induces a metabolic shift in microglia modulating the inflammatory response in vitro and in vivo. *Glia* **67**, 1047–1061 (2019).
30. Montilla, A. et al. Role of mitochondrial dynamics in microglial activation and metabolic switch. *ImmunoHorizons* **5**, 615–626 (2021).
31. Baik, S. H. et al. A Breakdown in metabolic reprogramming causes microglia dysfunction in Alzheimer's disease. *Cell Metab.* **30**, 493–507.e6 (2019).
32. Maes, M. E. et al. Mitochondrial network adaptations of microglia reveal sex-specific stress response after injury and UCP2 knockout. *iScience* **26**, 107780 (2023).
33. Hu, Y. et al. Dual roles of hexokinase 2 in shaping microglial function by gating glycolytic flux and mitochondrial activity. *Nat. Metab.* **4**, 1756–1774 (2022).
34. Stoolman, J. S. et al. Mitochondrial respiration in microglia is essential for response to demyelinating injury but not proliferation. *Nat. Metab.* **6**, 1492–1504 (2024).
35. Mora-Romero, B. et al. Microglia mitochondrial complex I deficiency during development induces glial dysfunction and early lethality. *Nat. Metab.* **6**, 1479–1491 (2024).
36. Peruzzotti-Jametti, L. et al. Mitochondrial complex I activity in microglia sustains neuroinflammation. *Nature* **628**, 195–203 (2024).
37. Pham, A. H., McCaffery, J. M. & Chan, D. C. Mouse lines with photoactivatable mitochondria to study mitochondrial dynamics. *Genesis* **50**, 833–843 (2012).
38. Bame, X. & Hill, R. A. Mitochondrial network reorganization and transient expansion during oligodendrocyte generation. *Nat. Commun.* **15**, 6979 (2024).
39. Quintana-Cabrera, R. & Scorrano, L. Determinants and outcomes of mitochondrial dynamics. *Mol. Cell* **83**, 857–876 (2023).
40. Hinkle, J. J., Olschowka, J. A., Love, T. M., Williams, J. P. & O'Banion, M. K. Cranial irradiation mediated spine loss is sex-specific and complement receptor-3 dependent in male mice. *Sci. Rep.* **9**, 18899 (2019).
41. Sipe, G. O. et al. Microglial P2Y12 is necessary for synaptic plasticity in mouse visual cortex. *Nat. Commun.* **7**, 10905 (2016).
42. Shapson-Coe, A. et al. A petavoxel fragment of human cerebral cortex reconstructed at nanoscale resolution. *Science* **384**, eadk4858 (2024).
43. Buchanan, J. et al. Oligodendrocyte precursor cells ingest axons in the mouse neocortex. *Proc. Natl. Acad. Sci. USA* **119**, e2202580119 (2022).
44. Eyo, U. B. & Wu, L.-J. Bidirectional microglia-neuron communication in the healthy brain. *Neural Plast.* **2013**, 456857 (2013).
45. Cserép, C. et al. Microglia monitor and protect neuronal function through specialized somatic purinergic junctions. *Science* **367**, 528–537 (2020).
46. Mehta, K., Chacko, L. A., Chug, M. K., Jhunjhunwala, S. & Ananthanarayanan, V. Association of mitochondria with microtubules inhibits mitochondrial fission by precluding assembly of the fission protein Dnm1. *J. Biol. Chem.* **294**, 3385–3396 (2019).
47. Shah, M., Chacko, L. A., Joseph, J. P. & Ananthanarayanan, V. Mitochondrial dynamics, positioning and function mediated by cytoskeletal interactions. *Cell. Mol. Life Sci.* **78**, 3969–3986 (2021).
48. Melkov, A. & Abdu, U. Regulation of long-distance transport of mitochondria along microtubules. *Cell. Mol. Life Sci.* **75**, 163–176 (2018).
49. Fang, J., Luo, S. & Lu, Z. H. K.2: Gatekeeping microglial activity by tuning glucose metabolism and mitochondrial functions. *Mol. Cell* **83**, 829–831 (2023).
50. Sabogal-Guáqueta, A. M. et al. Species-specific metabolic reprogramming in human and mouse microglia during inflammatory pathway induction. *Nat. Commun.* **14**, 6454 (2023).
51. Baik, S. H. et al. Hexokinase dissociation from mitochondria promotes oligomerization of VDAC that facilitates NLRP3 inflammasome assembly and activation. *Sci. Immunol.* **8**, eade7652 (2023).
52. Codocedo, J. F. et al. Therapeutic targeting of immunometabolism reveals a critical reliance on hexokinase 2 dosage for microglial activation and Alzheimer's progression. *Cell Rep.* **43**, 114488 (2024).
53. Fairley, L. H. et al. Mitochondrial control of microglial phagocytosis by the translocator protein and hexokinase 2 in Alzheimer's disease. *Proc. Natl. Acad. Sci. USA* **120**, e2209177120 (2023).
54. Leng, L. et al. Microglial hexokinase 2 deficiency increases ATP generation through lipid metabolism leading to β -amyloid clearance. *Nat. Metab.* **4**, 1287–1305 (2022).
55. Rabbani, N. & Thornalley, P. J. Hexokinase-2 glycolytic overload in diabetes and ischemia-reperfusion injury. *Trends Endocrinol. Metab.* **30**, 419–431 (2019).
56. Zhang, Y. et al. An RNA-sequencing transcriptome and splicing database of glia, neurons, and vascular cells of the cerebral cortex. *J. Neurosci.* **34**, 11929–11947 (2014).
57. Zhang, Y. et al. Purification and characterization of progenitor and mature human astrocytes reveals transcriptional and functional differences with mouse. *Neuron* **89**, 37–53 (2016).
58. Bernier, L.-P. et al. Nanoscale surveillance of the brain by microglia via cAMP-regulated filopodia. *Cell Rep.* **27**, 2895–2908.e4 (2019).
59. Stowell, R. D. et al. Noradrenergic signaling in the wakeful state inhibits microglial surveillance and synaptic plasticity in the mouse visual cortex. *Nat. Neurosci.* **22**, 1782–1792 (2019).
60. Liu, Y. U. et al. Neuronal network activity controls microglial process surveillance in awake mice via norepinephrine signaling. *Nat. Neurosci.* **22**, 1771–1781 (2019).
61. Aldana, B. I. Microglia-specific metabolic changes in neurodegeneration. *J. Mol. Biol.* **431**, 1830–1842 (2019).
62. Bernier, L.-P. et al. Microglial metabolic flexibility supports immune surveillance of the brain parenchyma. *Nat. Commun.* **11**, 1559 (2020).
63. Bernier, L.-P., York, E. M. & MacVicar, B. A. Immunometabolism in the brain: how metabolism shapes microglial function. *Trends Neurosci.* **43**, 854–869 (2020).
64. Kalsbeek, M. J. T., Mulder, L. & Yi, C.-X. Microglia energy metabolism in metabolic disorder. *Mol. Cell. Endocrinol.* **438**, 27–35 (2016).
65. Misgeld, T. & Schwarz, T. L. Mitostasis in neurons: maintaining mitochondria in an extended cellular architecture. *Neuron* **96**, 651–666 (2017).
66. Faitg, J. et al. 3D neuronal mitochondrial morphology in axons, dendrites, and somata of the aging mouse hippocampus. *Cell Rep.* **36**, 109509 (2021).
67. Jackson, J. G. & Robinson, M. B. Regulation of mitochondrial dynamics in astrocytes: mechanisms, consequences, and unknowns. *Glia* **66**, 1213–1234 (2018).
68. Uhlemann, R. et al. Actin dynamics shape microglia effector functions. *Brain Struct. Funct.* **221**, 2717–2734 (2016).
69. Möller, K. et al. A role for the centrosome in regulating the rate of neuronal efferocytosis by microglia in vivo. *eLife* **11**, e82094 (2022).

70. Han, S. M., Baig, H. S. & Hammarlund, M. Mitochondria localize to injured axons to support regeneration. *Neuron* **92**, 1308–1323 (2016).
71. Spillane, M., Ketschek, A., Merianda, T. T., Twiss, J. L. & Gallo, G. Mitochondria coordinate sites of axon branching through localized intra-axonal protein synthesis. *Cell Rep.* **5**, 1564–1575 (2013).
72. Cunniff, B., McKenzie, A. J., Heintz, N. H. & Howe, A. K. AMPK activity regulates trafficking of mitochondria to the leading edge during cell migration and matrix invasion. *Mol. Biol. Cell* **27**, 2662–2674 (2016).
73. Desai, S. P., Bhatia, S. N., Toner, M. & Irimia, D. Mitochondrial localization and the persistent migration of epithelial cancer cells. *Biophys. J.* **104**, 2077–2088 (2013).
74. Crosas-Molist, E. et al. AMPK is a mechano-metabolic sensor linking cell adhesion and mitochondrial dynamics to Myosin-dependent cell migration. *Nat. Commun.* **14**, 2740 (2023).
75. Shneyer, B. I., Ušaj, M., Wiesel-Motiuk, N., Regev, R. & Henn, A. ROS induced distribution of mitochondria to filopodia by Myo19 depends on a class specific tryptophan in the motor domain. *Sci. Rep.* **7**, 11577 (2017).
76. Kelly, B. & O'Neill, L. A. Metabolic reprogramming in macrophages and dendritic cells in innate immunity. *Cell Res.* **25**, 771–784 (2015).
77. Voloboueva, L. A., Emery, J. F., Sun, X. & Giffard, R. G. Inflammatory response of microglial BV-2 cells includes a glycolytic shift and is modulated by mitochondrial glucose-regulated protein 75/mortalin. *FEBS Lett.* **587**, 756–762 (2013).
78. Paolicelli, R. C. & Pluchino, S. Complex roles for mitochondrial complexes in microglia. *Nat. Metab.* **6**, 1426–1428 (2024).
79. He, D. et al. Disruption of the IL-33-ST2-AKT signaling axis impairs neurodevelopment by inhibiting microglial metabolic adaptation and phagocytic function. *Immunity* **55**, 159–173.e9 (2022).
80. Yona, S. et al. Fate mapping reveals origins and dynamics of monocytes and tissue macrophages under homeostasis. *Immunity* **38**, 79–91 (2013).
81. Madisen, L. et al. A robust and high-throughput Cre reporting and characterization system for the whole mouse brain. *Nat. Neurosci.* **13**, 133–140 (2010).
82. Hutchison, V., Lynch, A., Gutierrez-Gamez, A. M. & Chen, J. Inducible tricolor reporter mouse for parallel imaging of lysosomes, mitochondria, and microtubules. *J. Cell Biol.* **223**, e202305086 (2023).
83. Jackson, S. J. et al. Does age matter? The impact of rodent age on study outcomes. *Lab. Anim.* **51**, 160–169 (2017).
84. Chapman, T. W., Olveda, G. E., Bame, X., Pereira, E. & Hill, R. A. Oligodendrocyte death initiates synchronous remyelination to restore cortical myelin patterns in mice. *Nat. Neurosci.* **26**, 555–569 (2023).
85. Olveda, G. E., Barasa, M. N. & Hill, R. A. Microglial phagocytosis of single dying oligodendrocytes is mediated by CX3CR1 but not MERTK. *Cell Rep.* **43**, 114385 (2024).
86. Berger, D. R., Seung, H. S. & Lichtman, J. W. VAST (Volume Annotation and Segmentation Tool): efficient manual and semi-automatic labeling of large 3d image stacks. *Front. Neural Circuits* **12**, 88 (2018).
87. Fiji Downloads. *ImageJ Wiki* <https://imagej.github.io/software/fiji/downloads>.
88. MATLAB version: 24.1.0 (R2024a). *Natick, Massachusetts: The MathWorks Inc.* <https://www.mathworks.com> (2024)
89. 3D Slicer image computing platform. *3D Slicer* <https://slicer.org/>.
90. Kikinis, R., Pieper, S. D. & Vosburgh, K. G. 3D slicer: a platform for subject-specific image analysis, visualization, and clinical support. In *Intraoperative Imaging and Image-Guided Therapy* (ed. Jolesz, F. A.) 277–289 (Springer, New York, 2014).
91. Kapur, T. et al. Increasing the impact of medical image computing using community-based open-access hackathons: the NA-MIC and 3D Slicer experience. *Med. Image Anal.* **33**, 176–180 (2016).
92. Fedorov, A. et al. 3D slicer as an image computing platform for the quantitative imaging network. *Magn. Reson. Imaging* **30**, 1323–1341 (2012).
93. Ershov, D. et al. TrackMate 7: integrating state-of-the-art segmentation algorithms into tracking pipelines. *Nat. Methods* **19**, 829–832 (2022).
94. Ohsawa, K. et al. P2Y12 receptor-mediated integrin-beta1 activation regulates microglial process extension induced by ATP. *Glia* **58**, 790–801 (2010).

Acknowledgements

We would like to thank past and current members of the Hill and Hoppa laboratories at Dartmouth College for their valuable feedback and support throughout the project. We also thank Andrew D. McCray for helping with data analysis. This study was supported by National Institutes of Health grant R01NS122800, diversity supplement R01NS122800-S1, and the Esther A. & Joseph Klingenstein Fund and Simons Foundation to R.A.H; and the American Heart Association grant, 23PRE1018862, <https://doi.org/10.58275/AHA.23PRE1018862.pc.gr.161154> to Xh.B.

Author contributions

A.N.P. and R.A.H. conceived, designed and performed all the experiments, and most of the data analysis, quantification, and writing of the manuscript. Xh. B. performed the analyses and quantification for the TOMM20 immunostaining and the microglial process and mitochondrial motility. M.E.D. contributed to the analysis and quantification of microglia and their mitochondria from the publicly available H01 electron microscopy dataset. K.E.S. performed immunostaining and analyses of hexokinase 2 and 3. Xh.B., M.E.D., and K.E.S. contributed to data representation and writing pertaining to the respective analyses performed. A.N.P. and R.A.H. secured funding, and R.A.H. supervised the study.

Competing interests

The authors declare no competing interests.

Additional information

Supplementary information The online version contains supplementary material available at <https://doi.org/10.1038/s41467-025-66708-6>.

Correspondence and requests for materials should be addressed to Robert A. Hill.

Peer review information *Nature Communications* thanks Sandra Siegert and the other anonymous reviewer(s) for their contribution to the peer review of this work. A peer review file is available.

Reprints and permissions information is available at <http://www.nature.com/reprints>

Publisher's note Springer Nature remains neutral with regard to jurisdictional claims in published maps and institutional affiliations.

Open Access This article is licensed under a Creative Commons Attribution-NonCommercial-NoDerivatives 4.0 International License, which permits any non-commercial use, sharing, distribution and reproduction in any medium or format, as long as you give appropriate credit to the original author(s) and the source, provide a link to the Creative Commons licence, and indicate if you modified the licensed material. You do not have permission under this licence to share adapted material derived from this article or parts of it. The images or other third party material in this article are included in the article's Creative Commons licence, unless indicated otherwise in a credit line to the material. If material is not included in the article's Creative Commons licence and your intended use is not permitted by statutory regulation or exceeds the permitted use, you will need to obtain permission directly from the copyright holder. To view a copy of this licence, visit <http://creativecommons.org/licenses/by-nc-nd/4.0/>.

© The Author(s) 2025